https://doi.org/10.1093/plcell/koad319 THE PLANT CELL 2024: 36: 1007–1035

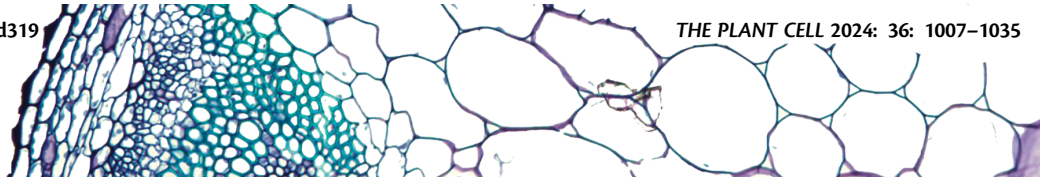

Research Article

Interplay of EXO70 and MLO proteins modulates trichome cell wall composition and susceptibility to powdery mildew

Jan W. Huebbers [1,†] George A. Caldarescu [2,†] Zdeňka Kubátová [2] Peter Sabol [2] Sophie C.J. Levecque [1] Hannah Kuhn [1] Ivan Kulich [2,‡] Anja Reinstädler [1] Kim Büttgen [1] Alba Manga-Robles [3] Hugo Mélida [3] Markus Pauly [4] Ralph Panstruga [1,*] and Viktor Žárský [2,5,*]

1 Unit of Plant Molecular Cell Biology, Institute for Biology I, RWTH Aachen University, Worringerweg 1, 52056 Aachen, Germany
2 Department of Experimental Plant Biology, Faculty of Science, Charles University, Viničná 5, 128 44 Prague, Czech Republic
3 Área de Fisiología Vegetal, Departamento de Ingeniería y Ciencias Agrarias, Universidad de León, 24071 León, Spain
4 Institute for Plant Cell Biology and Biotechnology, Heinrich-Heine-University Düsseldorf, Universitätsstr. 1, 40225 Düsseldorf, Germany
5 Institute of Experimental Botany of the Czech Academy of Sciences, Laboratory of Cell Biology, Rozvojová 263, 165 02 Prague 6 Lysolaje, Czech Republic

*Author for correspondence: panstruga@bio1.rwth-aachen.de (R.P.), viktor.zarsky@natur.cuni.cz (V.Ž.)
†These authors contributed equally to this work.
‡Present address: Institute for Science and Technology Austria (ISTA), Am Campus 1, 3400 Klosterneuburg, Austria.
The authors responsible for distribution of materials integral to the findings presented in this article in accordance with the policy described in the Instructions for Authors (https://academic.oup.com/plcell/pages/General-Instructions) are: Ralph Panstruga (panstruga@bio1.rwth-aachen.de) and Viktor Žárský (viktor.zarsky@natur.cuni.cz).

Abstract

Exocyst component of 70-kDa (EXO70) proteins are constituents of the exocyst complex implicated in vesicle tethering during exocytosis. MILDEW RESISTANCE LOCUS O (MLO) proteins are plant-specific calcium channels and some MLO isoforms enable fungal powdery mildew pathogenesis. We here detected an unexpected phenotypic overlap of *Arabidopsis thaliana exo70H4* and *mlo2 mlo6 mlo12* triple mutant plants regarding the biogenesis of leaf trichome secondary cell walls. Biochemical and Fourier transform infrared spectroscopic analyses corroborated deficiencies in the composition of trichome cell walls in these mutants. Transgenic lines expressing fluorophore-tagged EXO70H4 and MLO exhibited extensive colocalization of these proteins. Furthermore, mCherry-EXO70H4 mislocalized in trichomes of the *mlo* triple mutant and, vice versa, MLO6-GFP mislocalized in trichomes of the *exo70H4* mutant. Expression of GFP-marked PMR4 callose synthase, a known cargo of EXO70H4-dependent exocytosis, revealed reduced cell wall delivery of GFP-PMR4 in trichomes of *mlo* triple mutant plants. In vivo protein–protein interaction assays in plant and yeast cells uncovered isoform-preferential interactions between EXO70.2 subfamily members and MLO proteins. Finally, *exo70H4* and *mlo6* mutants, when combined, showed synergistically enhanced resistance to powdery mildew attack. Taken together, our data point to an isoform-specific interplay of EXO70 and MLO proteins in the modulation of trichome cell wall biogenesis and powdery mildew susceptibility.

Received September 07, 2023. Accepted December 15, 2023. Advance access publication December 20, 2023

IN A NUTSHELL

Background: MLO (Mildew resistance Locus O) proteins reside in the plasma membrane of plant cells. Some of these MLO proteins are known for conferring susceptibility to the fungal powdery mildew disease. MLO proteins are also linked to the targeted delivery of proteins to the extracellular space, a process termed exocytosis. EXO70 proteins form another protein family that plays a role in exocytosis. These proteins are part of a larger protein complex, called the exocyst. The exocyst mediates the docking of intracellular membrane-covered and cargo-bearing bubbles (vesicles) to the cellular plasma membrane. The cargo transported by such vesicles also includes materials to build cell walls.

Question: Do MLO and EXO70 proteins cooperate in the targeted deposition of cell wall components in leaf hairs (trichomes) of the model plant species *Arabidopsis thaliana*? Do EXO70 proteins, like MLO proteins, promote powdery mildew infection in *A. thaliana*?

Findings: Compared to normal control (wild-type) plants, trichomes on mutant plants that lack 3 distinct MLO proteins or the EXO70 protein EXO70H4 showed severe defects in the targeted deposition of the cell wall carbohydrate callose. Moreover, trichomes on these mutants exhibited an altered composition of their cell wall. The notion that the 3 MLO proteins and EXO70H4 work together during exocytosis was further spurred by the observation that these proteins interact with each other. Furthermore, the colonization of leaves by the powdery mildew fungus was reduced in plants missing EXO70H4 and either MLO2 or MLO6 compared to wild-type control plants.

Next steps: Our work demonstrates that EXO70H4 cooperates with 3 distinct MLO proteins in trichomes for the targeted deposition of cell wall building blocks. As the *A. thaliana* genome encodes 23 EXO70 proteins and 15 MLO proteins, we will investigate whether specific EXO70–MLO couples exist. These pairs may mediate localized secretion in different tissues or cell types.

Introduction

The exocyst is an evolutionarily conserved multisubunit protein complex found in all eukaryotes. It consists of 8 subunits (SEC3, SEC5, SEC6, SEC8, SEC10, SEC15, EXO70, EXO84) that together form a heterooligomeric complex (TerBush et al. 1996). Initially described in baker's yeast (*Saccharomyces cerevisiae*; TerBush et al. 1996), it was later examined in all eukaryotes, including plants (Elias et al. 2003). Exocyst is a CATCHR (complexes associated with tethering containing helical rods) type vesicle tethering complex that is involved in the tethering and docking of post-Golgi secretory vesicles to the plasma membrane (PM) and in the regulation of soluble N-ethylmaleimide-sensitive-factor attachment receptor (SNARE) complex formation. These functions are critical for membrane fusion events, including vesicle fusion at the PM (Heider and Munson 2012). In addition to this conserved core function, individual subunits or subcomplexes have been shown to be involved in cellular processes such as autophagy and cytoskeleton regulation (Heider and Munson 2012).

In eukaryotes other than land plants, exocyst subunits are typically present as solitary isoforms encoded by single-copy genes. In contrast, in land plants the EXO70 subunit family expanded and diverged into 3 subfamilies (EXO70.1, EXO70.2, and EXO70.3) with rapidly evolving paralogs (Synek et al. 2006; Cvrčková et al. 2012; Žárský et al. 2020). For example, in the dicotyledonous reference plant *Arabidopsis thaliana*, there are 23 EXO70 isoforms, and in the monocotyledonous reference crop plant rice (*Oryza sativa*), there are more than 40 isoforms (Cvrčková et al. 2012). The EXO70 subunit is crucial for the attachment of the entire exocyst complex to membranes due to its interaction with specific membrane lipids (Synek et al. 2021) and its association with small GTPases of the Rho family (Rossi et al. 2020). Among other functions, plant EXO70 isoforms are involved in the localized secretion of PM and cell wall components in the root epidermis, seed coats, pollen tubes, and trichomes (Kulich et al. 2010; Fendrych et al. 2013; Sekereš et al. 2017; Kulich et al. 2018; Kubátová et al. 2019). Associated with this secretory pathway function, the exocyst complex, and especially specific EXO70.2 subfamily isoforms, participates in cellular defense/innate immunity (Žárský et al. 2020). In this context, they contribute considerably to the biogenesis of defensive cell wall appositions (papillae) and the formation of perifungal membranes (Pečenková et al. 2017; Žárský et al. 2020; Ortmannová et al. 2022). Therefore, it is not surprising that they are often targeted by pathogen-derived effector proteins in order to overcome plant host immunity (Fujisaki et al. 2015; Pečenková et al. 2017; Žárský et al. 2020).

Trichomes are unbranched or branched polarized outgrowths of epidermal cells that can be uni- or multicellular and are distributed on the surface of plant organs, including leaves. In the case of the branched single-celled trichomes of *A. thaliana* rosette leaves, their development is genetically well-characterized (Hülskamp et al. 1994; Folkers et al. 1997) and can be divided into 6 major stages: initiation (including DNA endoreduplication), polar expansion, branching, branch growth, diffuse growth, and cellular maturation (Szymanski et al. 1998). *EXO70H4* (*At3g09520*) is the eleventh most highly expressed gene in mature trichomes as compared to rosette leaves with trichomes removed (Jakoby et al. 2008). Recent studies (Kulich et al. 2015; Kulich et al. 2018) showed that EXO70H4 has an important role in

trichome maturation, in particular in the deposition of secondary cell walls, especially in the apical region. Mature trichomes of *exo70H4* loss-of-function mutants appear to be mechanically more flexible than wild-type (WT) trichomes. This phenotype is due to the thinner secondary cell wall of mutant trichomes, which is related to the absence of the inner callose-rich cell wall layer, leading to a decrease in cell wall autofluorescence in mature trichomes of *exo70H4* mutants as compared to WT plants.

These phenotypic deviations include also an absence of the callose-rich Ortmannian ring (OR) from the *exo70H4* mutant trichomes (Kulich et al. 2015). The OR is a structure observed in mature trichomes that is rich in the β-1-3-glucan polymer callose and that divides trichomes into 2 major domains—the apical and the basal one (Kulich et al. 2015; Kulich et al. 2018; Kubátová et al. 2019). These domains are characterized by a different PM lipid composition and the presence of different EXO70 isoforms. EXO70A1 is recruited by the basal domain, which is located below the OR, and EXO70H4 is recruited by the apical domain, which is positioned above the OR (Kubátová et al. 2019). Deviations in cell wall autofluorescence and cell wall thickness associated with the defect in callose deposition were observed in *exo70H4* mutant trichomes as compared to WT trichomes (Kulich et al. 2015). Only EXO70H4, but not the closely related EXO70H3, was able to rescue the aberrant callose deposition of *exo70H4* mutant trichomes, suggesting that EXO70H4 specifically is crucial for the correct docking and PM secretion of callose synthases (Kulich et al. 2018).

Loss-of-function mutations in the *Mildew resistance locus o* (*Mlo*) gene of barley (*Hordeum vulgare*) have been known for decades to confer durable resistance against all naturally occurring isolates of the barley powdery mildew pathogen, *Blumeria hordei* (Jørgensen 1992). The identification of barley *Mlo* (Büschges et al. 1997) revealed a medium-sized gene family (~10 to 20 paralogs per plant species) encoding plant-specific and sequence-diversified integral membrane proteins (Devoto et al. 1999; Kusch et al. 2016). Members of this family have been identified in a wide variety of mono- and dicotyledonous plant species (Devoto et al. 2003; Kusch et al. 2016), and natural or induced loss-of-function mutations of *Mlo* genes have facilitated breeding for powdery mildew resistance in crop species such as barley, wheat (*Triticum aestivum*), pea (*Pisum sativum*), and tomato (*Solanum lycopersicum*) (reviewed in Kusch and Panstruga 2017).

In the dicotyledonous model plant *A. thaliana*, for instance, loss-of-function of 3 (*MLO2*, *MLO6*, *MLO12*) of its 15 *MLO* genes is required to resemble the nearly complete resistance of barley *mlo* mutants (Consonni et al. 2006). Due to the unequal genetic redundancy of these genes, the encoded proteins contribute unevenly to the susceptibility of *A. thaliana* against the adapted powdery mildew pathogens *Golovinomyces orontii* and *Golovinomyces cichoracearum*. In this scenario, MLO2 (At1g11310) is the major contributor to susceptibility and MLO6 (At1g61560), as well as MLO12 (At2g39200), are minor contributors (Consonni et al. 2006). Along with a reduced susceptibility to powdery mildew disease, barley *mlo* and *A. thaliana mlo2 mlo6 mlo12* plants develop indiscriminate callose-rich depositions at the cell wall and feature spontaneous death of mesophyll cells that is associated with premature leaf senescence (Wolter et al. 1993; Piffanelli et al. 2002; Consonni et al. 2010). MLO2 further plays decisive roles both in the regulation of ozone sensitivity (Cui et al. 2018) and in mediating systemic acquired resistance, a form of induced and systemically acting plant defense (Gruner et al. 2018).

Mutations in the *POWDERY MILDEW RESISTANT* (*PMR*) genes have been associated with a reduced susceptibility (i.e. enhanced resistance) of *A. thaliana* against these fungal pathogens (Vogel and Somerville 2000). The respective forward genetics approaches aimed for PR1-independent defense mechanisms and, accordingly, it was not surprising when *PMR2* was identified to be allelic to *MLO2* (Consonni et al. 2006). All other *PMR* genes discovered so far (*PMR4*–*PMR6*) encode proteins involved in the biogenesis and/or modification of the cell wall (Vogel et al. 2002; Jacobs et al. 2003; Nishimura et al. 2003; Vogel et al. 2004). PMR4 (At4g03550) was shown to be a callose synthase (GSL5/CALS12; Jacobs et al. 2003; Nishimura et al. 2003), PMR5 (At5g58600) is a putative pectin *O*-acetyltransferase (Vogel et al. 2004; Chiniquy et al. 2019) and PMR6 (At3g54920) a pectate lyase (Vogel et al. 2002). Consequently, MLO2 and/or other MLO proteins may be likewise involved in processes that are important for cell wall biogenesis.

MLO proteins were recently reported to function as calcium channels (Gao et al. 2022). Though this finding revealed the long sought-after biochemical function of MLO proteins, it remains enigmatic how the calcium channel activity of MLO proteins relates to cellular processes and susceptibility to powdery mildew. Characteristic sequence features conserved among all MLO proteins are (i) a binding site for the ubiquitous calcium sensor calmodulin in the proximal part of the intracellular MLO carboxy terminus (Kim et al. 2002), and (ii) 4 invariant cysteine residues in 2 of the extracellular loops that likely form 2 disulfide bridges, crucial for the stability of MLO proteins (Elliott et al. 2005). Based upon phylogenetic analysis, MLOs were classified into 7 clades, of which clade IV (mainly monocotyledonous plants) and clade V (mainly dicotyledonous plants) MLO proteins confer powdery mildew susceptibility (Kusch et al. 2016). Several studies carried out in *A. thaliana* reported that MLO proteins aside from clade V are involved in processes linked to polar secretion. For example, *A. thaliana mlo4* and *mlo11* mutant plants display severe root curling in response to a tactile stimulus, indicating a defect in thigmomorphogenesis (Chen et al. 2009; Bidzinski et al. 2014). Moreover, MLO7 (female gametophyte), as well as MLO5 and MLO9 (male gametophyte), are involved in the interaction between the ovule and pollen tube, as loss-of-function of these MLO proteins causes defects in ovule targeting by the pollen tube and, thus, reduced fertility (Kessler et al. 2010; Meng et al. 2020; Ju et al. 2021).

We here detected by a variety of histochemical staining procedures an unexpected phenotypic overlap of *A. thaliana*

exo70H4 single and *mlo2 mlo6 mlo12* triple mutants regarding the biogenesis of trichome secondary cell walls. Prompted by this finding, we combined genetic analysis with biochemical, cell biological protein–protein interaction and phytopathological assays, which together revealed an interplay of MLO and EXO70 proteins in the modulation of trichome cell wall composition and powdery mildew susceptibility by regulating secretory processes at the PM.

Results

Two independent *mlo2 mlo6 mlo12* triple mutants exhibit similar trichome cell wall phenotypes as seen in the *exo70H4-1* mutant

While inspecting aniline blue-stained leaf specimens in the context of plant-powdery mildew pathogenicity assays, we noticed that the rosette leaf trichomes of *mlo2-5 mlo6-2 mlo12-1* and *mlo2-6 mlo-6-4 mlo12-8* triple mutant plants exhibited a delocalized callose phenotype that was reminiscent of the previously reported aberrant callose deposition pattern seen in trichomes of the exocyst subunit *exo70H4-1* mutant (Kulich et al. 2015; Kulich et al. 2018). To assess this feature quantitatively, we defined 3 distinctive trichome callose phenotype categories (confined, erratic, and absent; Fig. 1) and determined the percentage of trichomes belonging to each of the categories for each mutant genotype, including a corresponding Col-0 WT control (Fig. 1A). Though we attempted to score primarily mature trichomes in this analysis, we cannot rule out that in some cases also slightly younger trichomes were included in the evaluation, because the distribution of trichomes of different developmental stages along the rosette leaf axis does not follow a simple pattern (Hülskamp et al. 1994). We found that ∼68% of the rosette leaf trichomes in Col-0 showed confined callose deposition, which was characterized by aniline blue-based fluorescence of the OR region with or without additional fluorescence in trichome branches. In addition, ∼14% of the WT trichomes exhibited a delocalized (erratic) callose pattern and ∼17% lacked any detectable fluorescence (absent callose deposition), possibly due to different developmental stages of the inspected trichomes (Fig. 1B). By contrast, the *exo70H4-1* mutant exhibited a drastically altered trichome staining pattern (<1% confined, ∼28% erratic, and ∼72% absent callose deposition, respectively) as reported previously (Kulich et al. 2015; Kulich et al. 2018). This phenotypic deviation was shared by the 2 *mlo* triple mutants, which showed a similar alteration of the callose fluorescence pattern (*mlo2-5 mlo6-2 mlo12-1*: ∼2% confined, ∼48% erratic, and ∼50% absent callose deposition, respectively; *mlo2-6 mlo-6-4 mlo12-8*: ∼7% confined, ∼32% erratic, and ∼61% absent callose deposition, respectively; Fig. 1B).

Inspired by the parallels in trichome-associated callose deposition phenotypes among the *exo70H4-1* mutant and the 2 *mlo* triple mutants, we explored whether the trichomes of these mutants exhibit further commonalities. To this end, we next measured cell wall autofluorescence (Fig. 1, C and D) and cell wall thickness (Fig. 1E) and observed that the trichomes of the *exo70H4-1* mutant and the 2 *mlo2 mlo6 mlo12* triple mutants showed significantly less autofluorescence than those of Col-0 WT plants (Fig. 1, C and D). Similarly, we found that the trichomes of all 3 investigated mutant genotypes developed significantly thinner cell walls than Col-0 WT trichomes (Fig. 1E).

We next used histochemical staining of rosette leaves of the above-described WT and mutant genotypes to examine the in situ accumulation of reactive oxygen species (ROS) and heavy metals in leaf trichomes. We chose these 2 features since trichomes of the *exo70H4-1* mutant were previously found to have defects in the accumulation of ROS (Kubátová, personal communication) and heavy metals (Kulich et al. 2015). As described above for the callose staining pattern (Fig. 1, A and B), we defined phenotypic categories (confined, diffuse, and absent) for these features and determined the proportion of trichomes in each category for each histochemical dye and genotype (Fig. 2). Upon staining the specimens with 3,3′-diaminobenzidine (DAB) to visualize ROS accumulation, we observed that the majority (∼53%) of Col-0 WT trichomes exhibited a confined region of ROS localization in the basal part of the trichomes, coinciding with the presumed location of the OR. A substantial portion (∼43%) of Col-0 trichomes also lacked detectable ROS accumulation, although sometimes weak staining was seen in branch tips. Only a minority (∼3%) showed a diffuse ROS pattern, which was characterized by a broader dispersal extending into the branching regions of the trichomes (Fig. 2, A and B). By contrast, *exo70H4-1* mutant plants largely either lacked any ROS accumulation in the trichomes (∼59%) or displayed a diffuse ROS distribution (∼39%). The same was essentially true for the 2 *mlo2 mlo6 mlo12* triple mutants, which, like the *exo70H4-1* mutant, showed a phenotypic pattern that differed from Col-0 WT trichomes in a statistically significant manner (Fig. 2B).

The histochemical analysis of heavy metal deposition assayed by diphenylthiocarbazone (dithizone) staining (Fig. 2, C and D) revealed similar deviations as the DAB staining for ROS accumulation described above. Leaf trichomes of Col-0 WT plants showed either confined, ring-like staining of the basal trichome regions (∼30%) or no staining (∼50%), and only rarely exhibited diffuse staining (∼16%). Differing from this distribution, trichomes of the *exo70H4-1* single mutant and the 2 *mlo2 mlo6 mlo12* triple mutants had a greater proportion of diffuse staining (>40%), which in all cases was different from Col-0 WT in a statistically significant manner (Fig. 2D). Collectively, these assays revealed an unexpected phenotypic overlap between the *exo70H4-1* mutant and *mlo2 mlo6 mlo12* triple mutants that pointed to shared alterations in trichome cell wall architecture of these mutants and therefore to a common/shared function of the associated proteins in trichome cell wall biogenesis and/or trichome maturation.

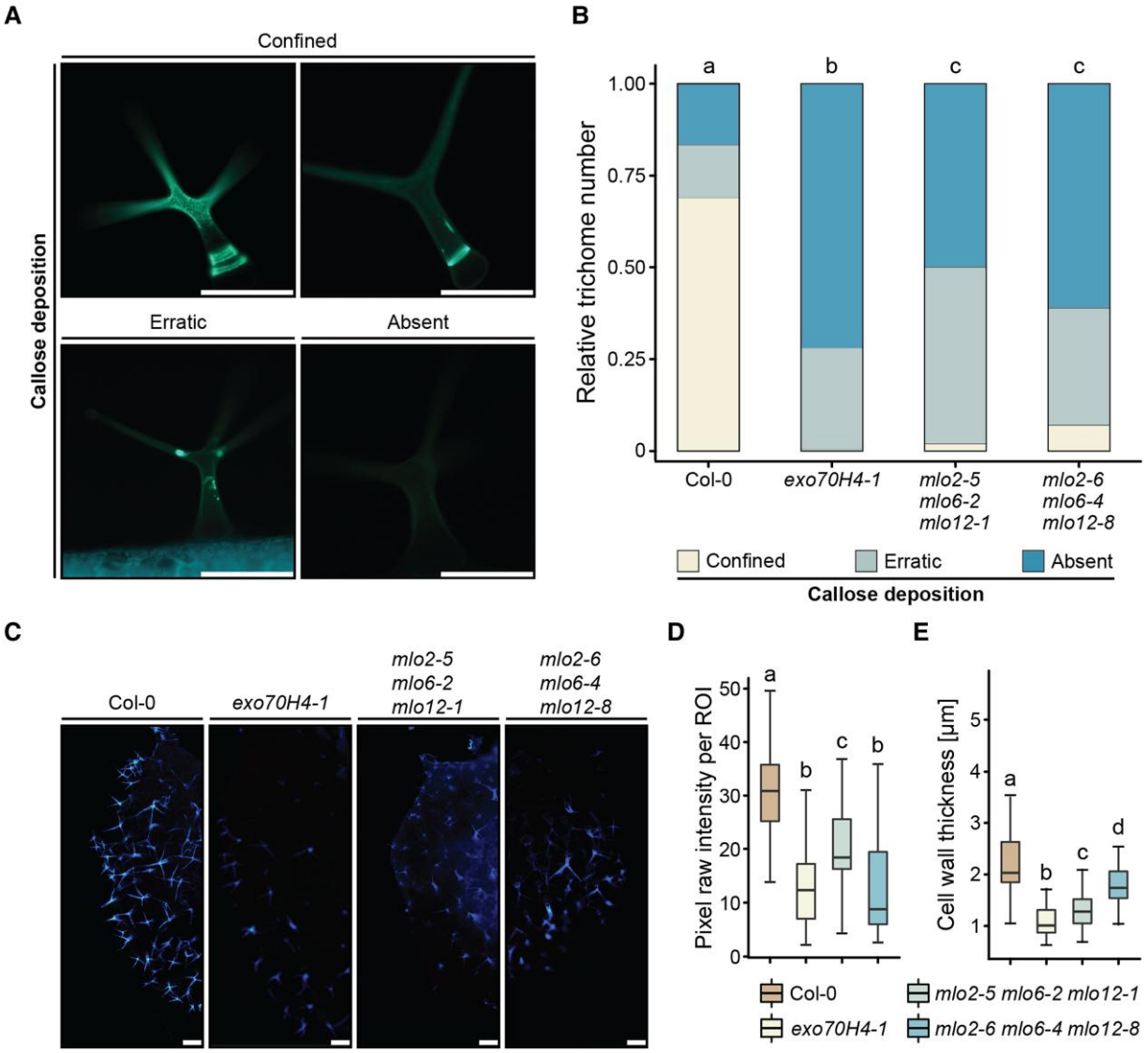

Figure 1. The *exo70H4-1* mutant and 2 independent *mlo2 mlo6 mlo12* triple mutants share similar rosette leaf trichome phenotypes. **A)** Representative micrographs illustrating the trichome-associated callose phenotype categories (confined, erratic, and absent) following staining with aniline blue. **B)** Frequencies of trichome callose patterns defined in **A)** in trichomes of Col-0 WT and the indicated mutants following staining with aniline blue. Values are based on 4 experiments with ~150 trichomes inspected per experiment and genotype, i.e. ~600 trichomes per genotype in total. Data were analyzed by chi-square test, the *P*-values were corrected by FDR ($\alpha = 0.05$), and letters denote statistically significant differences between genotypes. **C)** Representative micrographs depicting trichome cell wall autofluorescence in rosette leaves of Col-0 WT plants and the indicated mutant plants. **D)** Quantification of trichome cell wall autofluorescence. Shown is the pixel intensity per randomly chosen regions of interest (ROIs), calculated based on autofluorescence micrographs as those exemplarily shown in **C)**. Box plots represent the probability distribution of data as described in the Materials and methods section. Values are based on 2 experiments with ~20 trichomes inspected per experiment and genotype, i.e. ~40 trichomes per genotype in total. Letters assign differences of statistical significance (pairwise Wilcoxon–Mann–Whitney test corrected by FDR, $\alpha = 0.01$). **E)** Quantification of trichome cell wall thickness. Cell wall thickness was measured in proximity to the OR. Box plots represent the probability distribution of data as described in the Materials and methods section. Values are based on 4 experiments with ~20 trichomes inspected per experiment and genotype, i.e. ~80 trichomes per genotype in total. Letters represent differences of statistical significance (pairwise Wilcoxon–Mann–Whitney test corrected by FDR, $\alpha = 0.01$). Scale bars in **A)** and **C)** represent 200 μm.

Genetic analysis identifies mutations in *MLO2* and *MLO6* as the main cause of the aberrant trichome phenotypes in the *mlo* triple mutants

To assess whether the trichome phenotypic deviations observed with the 2 *mlo2 mlo6 mlo12* triple mutants were due to defects in one of the mutated *MLO* genes or the effect of 2 or all 3 mutations in combination, we performed some of the above-described assays with a selected subset of *mlo2*, *mlo6*, and *mlo12* single and double mutants. Following callose staining with aniline blue, we observed that the *mlo6-2* single mutant, as well as the *mlo2-5 mlo6-2* and *mlo6-2 mlo12-1* double mutants, showed a distribution pattern

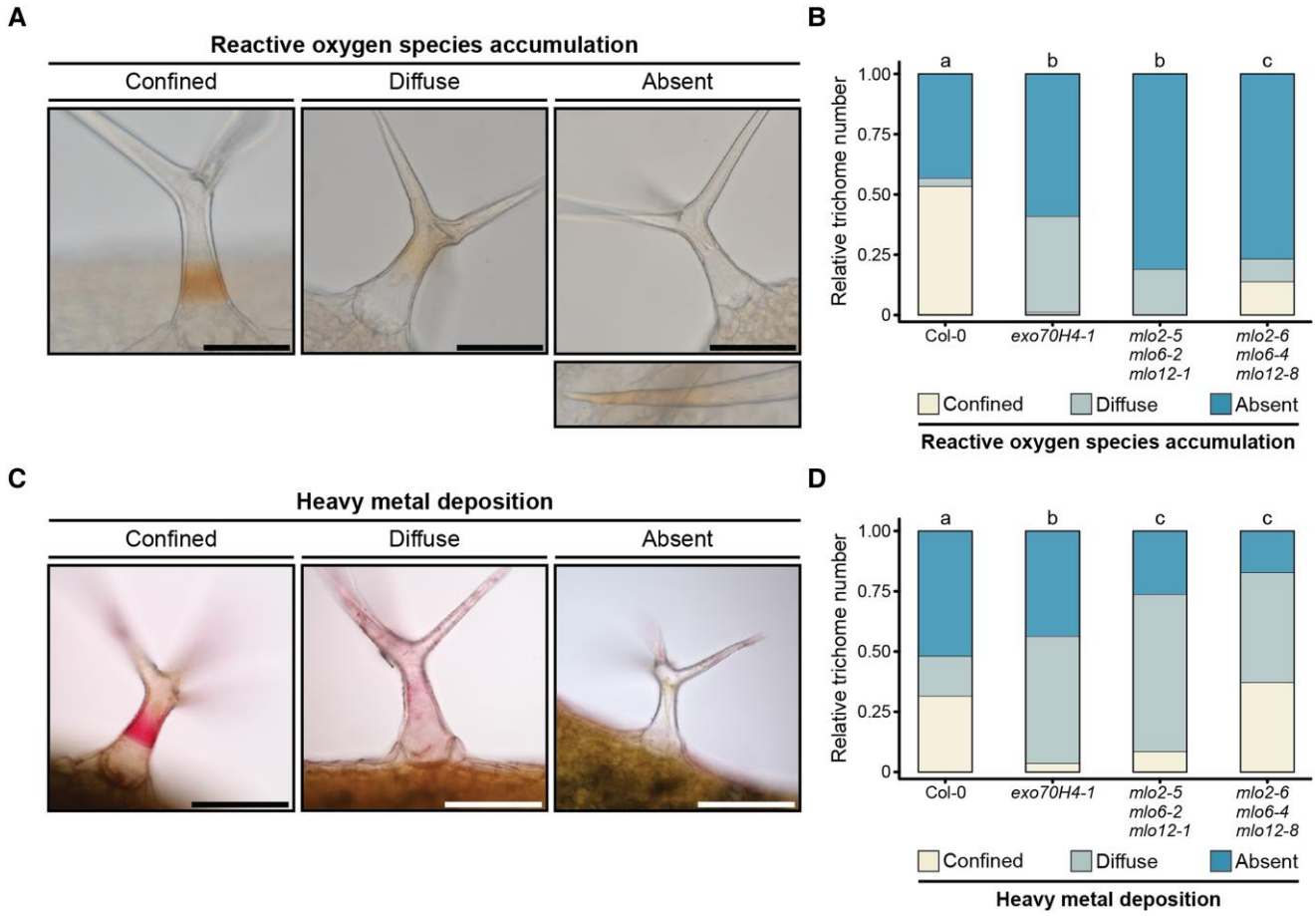

Figure 2. The *exo70H4-1* single mutant and the *mlo2 mlo6 mlo12* triple mutants share similar aberrant ROS and heavy metal localization patterns in rosette leaf trichomes. **A)** Representative micrographs illustrating categories of trichome-associated reactive oxygen species (ROS) occurrence (confined, diffuse, and absent). Trichomes lacking ROS accumulation in the basal part of the trichomes and the proximal areas of the branches occasionally exhibited weak DAB staining in the branch tips (see separate micrograph below the main panel). **B)** Frequencies of trichome ROS accumulation patterns as defined in **A)** in Col-0 WT and the indicated mutant plants. Values are based on 3 experiments with ∼50 trichomes inspected per experiment and genotype, i.e. ∼150 trichomes per genotype in total. Data were analyzed by chi-square test, the *P*-values were corrected by FDR ($\alpha = 0.05$), and letters denote statistically significant differences between genotypes. **C)** Representative micrographs illustrating categories of trichome-associated heavy metal phenotypes (confined, diffuse, and absent). **D)** Frequencies of trichome heavy metal deposition patterns defined in **C)** in Col-0 WT and the indicated mutant plants. Values are based on 3 experiments with ∼50 trichomes inspected per experiment and genotype, i.e. ∼150 trichomes per genotype in total. Data were analyzed by chi-square test, the *P*-values were corrected by FDR ($\alpha = 0.05$), and letters denote statistically significant differences between genotypes. Scale bars in **A)** and **C)** represent 200 μm.

that largely resembled the pattern of the 2 *mlo* triple mutants concerning the occurrence of erratic callose deposits or the absence of callose deposition. By contrast, the *mlo2-5* and *mlo12-1* single mutants as well as the *mlo2-5 mlo12-1* double mutant had a WT-like distribution of callose staining (Supplementary Fig. S1A). A similar tendency, yet less pronounced, was visible in assays of the thickness of trichome cell walls, with trichomes of the *mlo6-2* mutant and its derived double mutants showing the largest deviation from Col-0 WT trichomes (Supplementary Fig. S1B). Concerning ROS accumulation, trichomes of all *mlo* single and double mutants were significantly different from Col-0 WT trichomes (Supplementary Fig. S1C). Regarding trichome autofluorescence, all *mlo* single and double mutants apart from the *mlo2-5 mlo6-2* double mutant, which showed drastically reduced autofluorescence, exhibited a WT-like fluorescence intensity (Supplementary Fig. S1D). Finally, with respect to the accumulation of heavy metals in trichomes, particularly in trichomes of the *mlo2-5* single mutant and the *mlo2-5 mlo6-2* double mutant, we found distribution patterns that deviated from Col-0 WT and resembled the phenotype of *mlo* triple mutant plants (Supplementary Fig. S1E).

These outcomes were substantiated in an independent set of experiments in which we included an additional CRISPR-Cas9-derived *mlo6* null mutant allele, *mlo6-6* (Supplementary Fig. S2, A and B), in combination with various controls (Col-0 WT, *exo70H4-1* and *mlo6-2* mutants). Reminiscent of the *mlo6-2* mutant phenotype, the *mlo6-6* mutant exhibited aberrant callose deposition, cell wall

thickness, and autofluorescence in its rosette leaf trichomes (Supplementary Fig. S2, C to E). We further assessed *exo70H4-1 mlo2-5* and *exo70H4-1 mlo6-2* double mutants with respect to these features. The 2 double mutants behaved similarly to the *exo70H4-1* and *mlo6-2* single mutants, showing no further enhancement of the respective trichome phenotypes (Supplementary Fig. S2, C to E).

In sum, we noticed a variable contribution of the 3 *MLO* genes to the various trichome phenotypes. Nonetheless, a pivotal contribution of *MLO6*, alone or in combination with *MLO2*, emerged as a common theme across the different assays. However, due to the mixed and variable contributions of the 3 *MLO* genes to the different trichome phenotypes, we performed the following experiments with the 2 *mlo2 mlo6 mlo12* triple mutants for consistency.

Cell wall analysis of isolated trichomes provides evidence for altered cell wall composition in the *exo70H4-1* single mutant and the 2 *mlo* triple mutants

We next wondered whether the similar aberrations in *exo70H4-1* and *mlo2 mlo6 mlo12* mutant trichomes were symptoms of pervasive alterations of cell wall composition in these trichomes compared to the Col-0 WT. For global quantitative cell wall analyses, we first used histochemistry of isolated leaf trichomes to confirm that the cell wall deviations observed in *exo70H4-1* and *mlo2 mlo6 mlo12* leaf-resident trichomes were likewise detectable in detached trichomes (Fig. 3). We isolated trichomes via an established method for the gentle separation of rosette leaf tissue and trichomes (Huebbers et al. 2022) and stained the isolated trichomes with calcofluor white, which binds to unsubstituted β-glucan polymers such as cellulose or callose (Eschrich and Currier 1964; Wood 1980). A quantitative assessment by microscopy revealed that ∼64% of the Col-0 trichomes showed an OR-like structure in their basal regions (Fig. 3A). By contrast, trichomes isolated from *exo70H4-1* and *mlo2-5 mlo6-2 mlo12-1* mutant plants displayed a statistically significant reduction in OR formation, to ∼10% and ∼7% of the inspected trichomes, respectively. In contrast to leaf-attached trichomes (Fig. 1A), quantification of OR formation in isolated trichomes of *mlo2-6 mlo6-4 mlo12-8* mutant plants (∼52%) resembled the WT, possibly due to differences in dye uptake between leaf-associated and detached trichomes. In sum, the calcofluor white staining pattern of isolated trichomes was largely consistent with the aniline blue staining pattern of leaf-associated trichomes described above (Fig. 1, A and B).

We also stained the isolated trichomes with the colorimetric dyes ruthenium red (to visualize pectin) and toluidine blue O (to stain polygalacturonic acids pinkish-purple and polyaromatic substances such as lignin blue or greenish-blue, Pradhan Mitra and Loqué 2014). Though these stains did not show drastic differences in pectin or lignin content across the various genotypes, we encountered a striking segmentation pattern in ∼30% of the Col-0 trichomes following ruthenium red and toluidine blue O staining (Fig. 3, B and C). This pattern was characterized by a stained basal and an unstained apical trichome region, separated by a sharp boundary that differed in its position from the location of the OR. Unlike for WT trichomes, the formation of this clear segmentation was considerably reduced in *exo70H4-1-* (∼5%) and *mlo2-5 mlo6-2 mlo12-1* (∼3%)-derived trichomes, though this reduction was not statistically significant in the case of ruthenium red staining (Fig. 3B). Trichomes released from *mlo2-6 mlo6-4 mlo12-8* mutant plants, by contrast, occasionally (∼17%) exhibited a WT-like segmentation pattern, accompanied by a higher degree of variation across the experiments (Fig. 3, B and C).

We next used isolated WT and mutant trichomes for analytical quantification of cell wall matrix monosaccharides (rhamnose, arabinose, galactose, mannose, fucose, xylose, and glucose), uronic sugar acids, and crystalline cellulose (Fig. 4 and Supplementary Fig. S3). For most of the neutral monosaccharides analyzed, there was no marked difference in their levels between the mutants and Col-0 WT trichomes (Supplementary Fig. S3, A to E). Exceptions were arabinose and galactose, for which lower levels were found in trichomes of either the *mlo2-5 mlo6-2 mlo12-1* mutant (arabinose; not statistically significant; Fig. 4A) or the 2 *mlo* triple mutants (galactose; Fig. 4B). Taken together, these deviations caused a reduction in the sum of the neutral monosaccharides in the case of the *mlo2-5 mlo6-2 mlo12-1* mutant as compared to the other genotypes (Fig. 4C). Similar to most neutral monosaccharides, we also did not find any marked differences in crystalline cellulose content and the levels of uronic acids between mutant and Col-0 WT trichomes (Supplementary Fig. S3, F and G).

We subjected the same sample material used for the quantification of uronic acids to Fourier transform infrared (FTIR) spectroscopy for the global analysis of cell wall composition. Averaging of the retrieved spectra per genotype and visualization in a plot revealed notable differences among the genotypes tested (Supplementary Fig. S3H). Areas that stood out in this averaged plot included (i) a peak (indicating a reduction in comparison to Col-0) in the region of ∼1,500 cm^{-1} to ∼1,300 cm^{-1} prominent in all mutants, (ii) a peak between ∼1,200 cm^{-1} and ∼900 cm^{-1} in both *mlo* triple mutants accompanied by a high variability as indicated by the shaded area, and (iii) a peak at around 850 cm^{-1} in all mutants.

Then, the FTIR spectra of the individual measurements from 2 independent experiments (8 samples per genotype in total) were used for principal component analysis (PCA). A PCA plot of the first and second dimensions showed that dimension 1 and dimension 2 accounted for 42.2% and 25.4% of the variability within the data, respectively (Fig. 4D). The plot also indicated an overall genotype-specific clustering of the individual spectra, albeit 2 spectra of Col-0 trichomes grouped with the spectra retrieved from *mlo2-6 mlo6-4 mlo12-8* samples. Despite this minor deviation, we concluded that all mutant samples differ from the WT in dimension 1, whereas only *exo70H4-1* and *mlo2-5 mlo6-2 mlo12-1* samples, but not *mlo2-6 mlo6-4 mlo12-8* samples, varied also in dimension 2. The eigenvectors associated

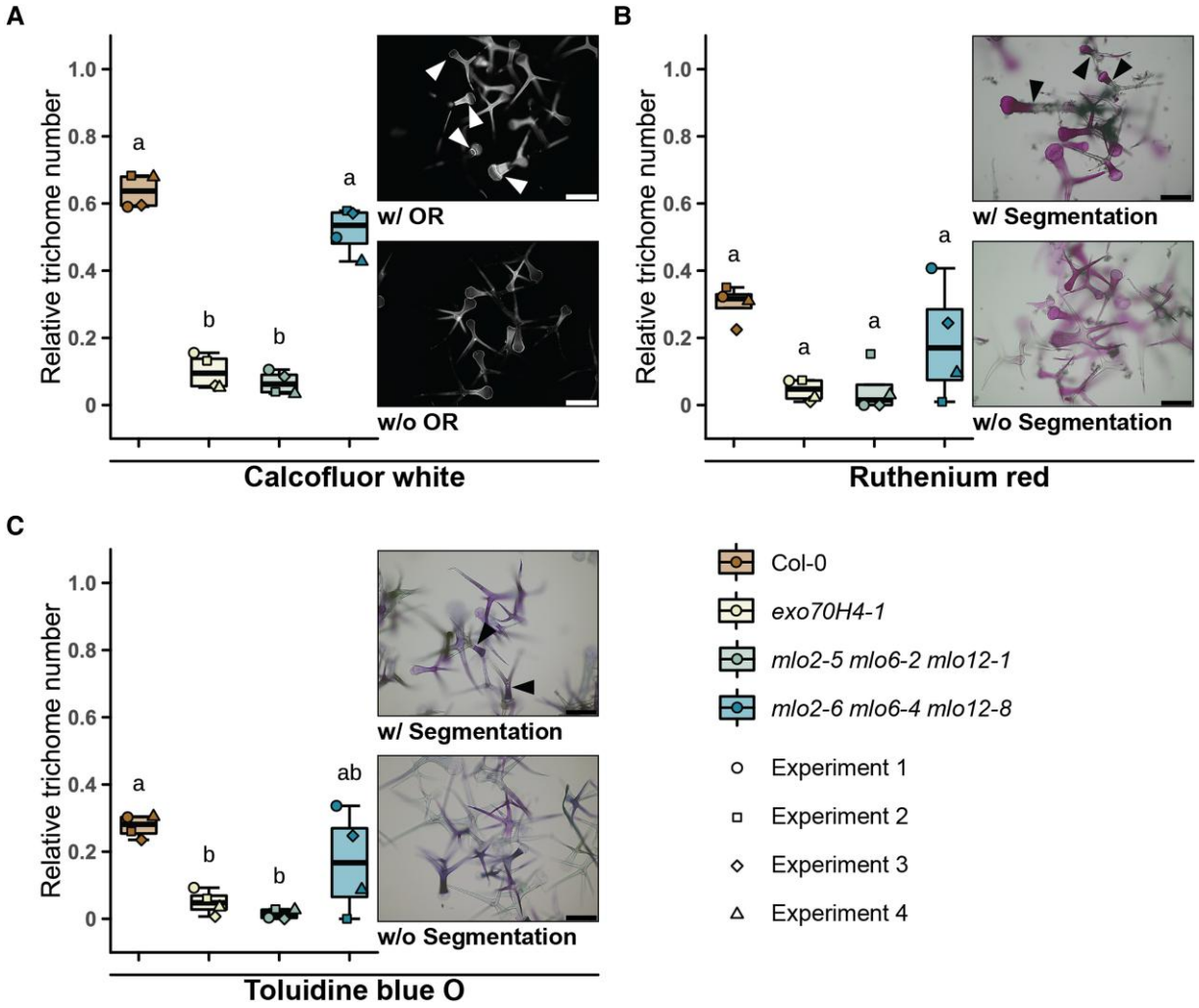

Figure 3. Histochemical staining of detached rosette leaf trichomes indicates a reduced frequency of cell wall segmentation in *exo70H4-1* and *mlo2 mlo6 mlo12* mutants. Trichomes were isolated from rosette leaves and stained as described in the Materials and methods section. **A)** Frequency of the OR upon calcofluor white staining. **B, C)** Frequency of basal-apical segmentation upon ruthenium red **B)** or toluidine blue O **C)** staining. Box plots represent the probability distribution of data as described in the Materials and methods section. Values are based on 4 independent experiments with 3 replicates each. About 100 trichomes were assessed per replicate, i.e. ~1,200 trichomes per genotype in total. Letters assign differences of statistical significance (pairwise Student's *t*-test corrected by FDR, $\alpha = 0.01$). Micrographs show stained trichomes with (w/, arrowheads) or without (w/o) the respective pattern. Note that in panel **B)**, there is no statistically significant difference between genotypes due to the stringent statistical analysis performed ($\alpha = 0.01$). Scale bars represent 200 μm.

with such wavenumbers that contributed the most to dimensions 1 and 2 are listed in Supplementary Table S1 and comprised values between 1,474 cm^{-1} and 1,425 cm^{-1} as well as values around 900 cm^{-1}, which are associated with cell wall constituents such as cellulose, pectin, and arabinogalactan. Altogether, the results of FTIR spectroscopy indicated global alterations in the cell walls of *exo70H4-1* single and *mlo* triple mutant trichomes.

Fluorophore-labeled EXO70H4 and MLO proteins co-localize in leaf trichomes

To study the subcellular localization of EXO70H4 and MLO proteins in rosette leaf trichomes, we transformed mCherry-EXO70H4-expressing plants in the Col-0-derived *rdr6* background (Kulich et al. 2018), which reduces transgene silencing, with constructs expressing GFP-tagged versions of MLO2, MLO6, or MLO12. All *MLO* genes were expressed under the control of the *EXO70H4* promoter (*ProEXO70H4*), which confers preferential expression in trichomes (Kulich et al. 2018). Inspection of the resulting transgenic lines by confocal laser scanning microscopy revealed that the MLO2-GFP fusion protein co-localized with mCherry-EXO70H4 in mature trichomes, mainly in the zone of the OR and above it at the PM delineating the thickened secondary cell wall. We also observed colocalization of the 2 proteins in the apical domain of the trichome PM. Here, MLO2-GFP co-localized with mCherry-EXO70H4 in PM speckles and the cell wall (Fig. 5, A and B). Similar subcellular

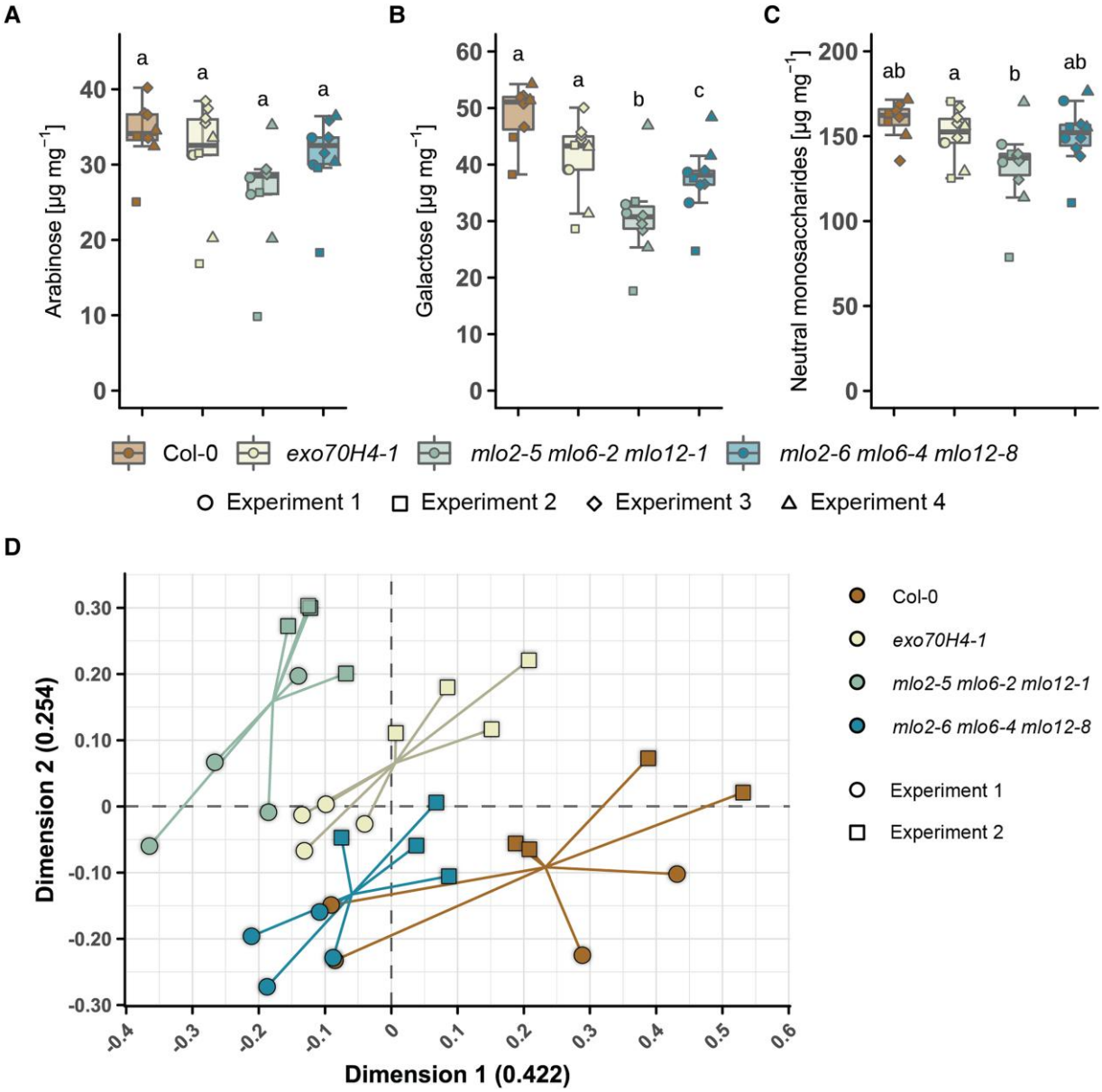

Figure 4. Cell walls of isolated *exo70H4-1* and *mlo2 mlo6 mlo12* triple mutant rosette leaf trichomes have altered carbohydrate composition. **A to C)** Quantification of neutral matrix monosaccharides in the indicated genotypes. Different geometric shapes denote samples that arose from the same independent experiment, as indicated in the legend below the box plots. **A, B)** Abundance of the neutral monosaccharides arabinose **A)** and galactose **B)** in the alcohol-insoluble residue recovered from trichomes of the various genotypes. Box plots represent the probability distribution of data as described in the Materials and methods section. Values are based on at least 3 independent experiments. Each independent experiment comprised at least 2 replicates, representing trichomes that were retrieved from the same round of trichome isolation. Letters assign differences of statistical significance (pairwise Student's *t*-test corrected by FDR, $\alpha = 0.05$). **C)** Total abundance of neutral monosaccharides in the cell wall matrix of the various genotypes. Box plots include the amounts of the monosaccharides indicated in panels **A)** and **B)** in addition to the abundance of rhamnose, mannose, fucose, xylose, and matrix glucose in the alcohol-insoluble residue (Supplementary Fig. S3A to E). Letters assign differences of statistical significance (pairwise Student's *t*-test corrected by FDR, $\alpha = 0.05$). **D)** Principal component analysis of FTIR spectra of rosette leaf trichomes isolated from the various genotypes (2 experiments with 4 samples each). The plot shows the first and second dimensions, which accounted for 42.2% and 25.4% of the variability between samples, respectively. The intersection point of the lines indicates the mean of the data points per genotype.

distribution patterns were observed for the MLO6-GFP and MLO12-GFP fusion proteins, which co-localized with mCherry-EXO70H4 at the OR region, in PM speckles and the cell wall (Fig. 5, A and B). We noticed that the colocalization of EXO70H4 and MLO proteins was independent of the developmental stage of the trichomes, as we detected similar colocalization patterns in trichomes derived from different rosette leaf areas (Supplementary Fig. S4).

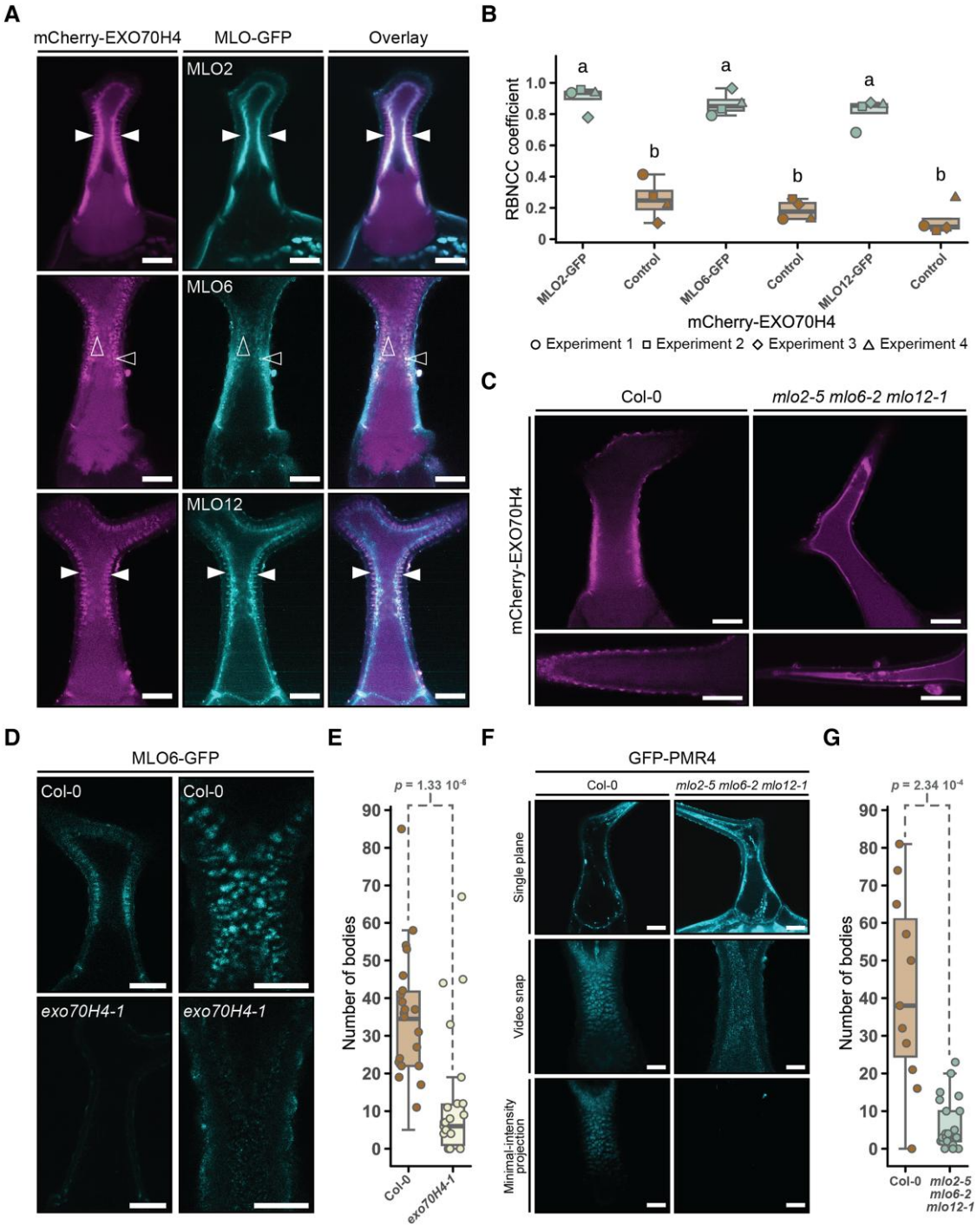

Figure 5. Subcellular localization of fluorophore-labeled EXO70H4, MLO, and PMR4 proteins in rosette leaf trichomes of *exo70H4* and *mlo2 mlo6 mlo12* transgenic lines. **A)** Colocalization of mCherry-EXO70H4 and GFP-tagged MLO proteins in trichomes of transgenic *A. thaliana* lines. mCherry-EXO70H4 and MLO-GFP (MLO2, MLO6, and MLO12) were expressed in transgenic *A. thaliana* lines (Col-0-derived *rdr6* background) under the control of the *EXO70H4* promoter. In each micrograph, a single confocal plane is shown. Filled and open arrowheads point to examples of the fluorophore-labeled cell wall channels and PM speckles, respectively. Note that the ellipsoid structures seen in the GFP channel in the case of the MLO2-GFP trichome likely are chloroplasts present in mesophyll cells beneath the trichome cell. Scale bars represent 20 μm. **B)** Replicate-Based Noise Corrected Correlation (RBNCC) coefficient, indicating a correlation between the localization of GFP-tagged MLO proteins and mCherry-EXO70H4 in mature trichomes of the transgenic lines shown in **A)**. Control values are based on rotating the mCherry images by 90 degrees counterclockwise. Box plots represent the probability distribution of data as described in the Materials and methods section. Values are based on micrographs taken in 4 experiments, with 5 trichomes per experiment and transgenic line. Letters assign differences of statistical significance (pairwise Wilcoxon–Mann–Whitney test corrected by FDR, $\alpha = 0.05$). **C)** Subcellular localization of mCherry-EXO70H4, expressed under the control of

(continued)

Notably, the speckled domain defined by MLO12-GFP appeared to be broader than the mCherry-EXO70H4 signal, which localized to its center, as if delimited by the MLO12-GFP protein as a boundary (Supplementary Fig. S5, A and B). Furthermore, we detected MLO12-GFP-labeled bodies in the cytoplasm. To our surprise, we observed both EXO70H4 and all 3 fluorescent MLO fusion proteins also in cell wall channels, which were oriented perpendicularly to the PM, and which could also be seen following plasmolysis (Fig. 5A and Supplementary Fig. S5C). This observation indicates the trapping of a portion of the fluorophore-labeled EXO70H4 and MLO proteins within the cell wall, a conclusion also supported by the visualization of membrane remnants within the cell wall as visualized by electron microscopy (Kubátová et al. 2019). Altogether, these data suggest that mCherry-EXO70H4 co-localizes with all 3 GFP-labeled MLO proteins tested, further highlighting the possibility that they might cooperate in the same cellular pathway and may even reside within the same macromolecular complex/compartment.

EXO70H4 and MLO proteins mutually impact each other's subcellular localization

Since EXO70H4 and MLO proteins co-localize substantially in trichomes, we next investigated whether they influence each other's localization. We transformed Col-0 WT plants and the *mlo2-5 mlo6-2 mlo12-1* mutant with the above-mentioned mCherry-EXO70H4 construct and compared the subcellular localization of the fluorescent fusion protein in mature trichomes of the resulting transformants. In transgenic Col-0 plants, we observed that the mCherry-EXO70H4 signal was mostly present at the PM and within the thickened secondary cell wall of the central trichome stalk region (Fig. 5C and Supplementary Fig. S5D). In addition, red fluorescence was localized at the cell wall papillae that decorate the surface of individual trichome branches. By contrast, mCherry-EXO70H4 exhibited predominantly cytoplasmic localization in *mlo2-5 mlo6-2 mlo12-1* transformants and was essentially absent from the PM and the cell wall, including its surface papillae (Fig. 5C and Supplementary Fig. S5D).

As the *mlo6-2* mutant most strongly resembled the aberrant trichome phenotypes of the *exo70H4-1* mutant (Supplementary Fig. S1), we focused on MLO6 to study whether the *exo70H4* mutation likewise affects the subcellular localization of MLO proteins. To this end, we stably expressed the MLO6-GFP fusion protein under the control of the native *MLO6* promoter (*ProMLO6*) in both Col-0 WT and *exo70H4-1* mutant plants. We noticed that in mature trichomes of transgenic Col-0 WT plants, MLO6-GFP seemed to localize primarily to the PM and the cell wall, including the above-described cell wall channels (Fig. 5D and Supplementary Fig. S5E), a pattern reminiscent of the pattern seen when co-expressed with mCherry-EXO70H4 in the *rdr6-1* mutant background (Fig. 5A). In addition, we detected the MLO6-GFP fusion protein in stationary PM-associated speckles in WT plants (Fig. 5, D and E, Supplementary Movie S1). By contrast, the MLO6-GFP fluorescent signal was less pronounced in the cell walls of *exo70H4-1* transgenic plants (Fig. 5D and Supplementary Fig. S5E), possibly due to the reduced thickness of trichome secondary cell walls in this genetic background (Kulich et al. 2015). Instead, MLO6-GFP was in part visible in the cytoplasm in this genotype. In addition, the PM-associated MLO6-GFP speckles were smaller and appeared more mobile in the *exo70H4-1* transgenic lines (Fig. 5E and Supplementary Movie S2). In summary, the data suggest that EXO7H4 and MLO proteins mutually impact each other's subcellular localization.

Fluorophore-tagged PMR4 callose synthase is mislocalized in transgenic *mlo2-5 mlo6-2 mlo12-1* triple mutant lines

Because of the similarities in aberrant callose deposition in the *exo70H4* and *mlo2-5 mlo6-2 mlo12-1* triple mutant (see above and Fig. 1), we decided to examine the subcellular localization and intracellular dynamics of the PMR4 callose synthase in the *mlo* triple mutant. PMR4 is responsible for callose deposition in *A. thaliana* trichomes and becomes delocalized in the

Figure 5. (Continued)
the *EXO70H4* promoter in either a transgenic Col-0 WT plant (left panels) or a *mlo2-5 mlo6-2 mlo12-1* triple mutant plant (right panels). The upper panels show the trichome stalk region, and the lower panels depict an individual trichome branch. Scale bars represent 20 μm. **D)** Subcellular localization of MLO6-GFP, expressed under the control of the *MLO6* promoter, in either a transgenic Col-0 WT plant (upper panels) or the *exo70H4-1* mutant plant (lower panels). The left panels show single planes focused on the cell wall, and the right panels show single planes focused on the PM. Scale bars represent 20 μm each. **E)** Quantification of the number of stationary MLO6-GFP-labeled intracellular dot-like compartments as calculated from the minimal-intensity projection images (see Materials and methods for further details). Box plots represent the probability distribution of data as described in the Materials and methods section. Values are based on 2 experiments with a total of 30 images analyzed per genotype. The *P*-value was computed according to Wilcoxon–Mann–Whitney and indicates the statistical difference between the mobility of MLO6-GFP in the Col-0 WT background and the *exo70H4-1* background. **F)** Subcellular localization of GFP-PMR4, expressed under the control of the *EXO70H4* promoter in either a transgenic Col-0 WT plant (left panels) or a *mlo2-5 mlo6-2 mlo12-1* triple mutant plant (right panels). The micrographs show a single confocal plane (upper panels), a snapshot from a time-series video (middle panels), and a minimal-intensity projection from the time series (bottom panels). Scale bars represent 20 μm. **G)** Quantification of the number of stationary GFP-PMR4-labeled intracellular dot-like compartments as calculated from minimal-intensity projection images (see Materials and methods for further details). Box plots represent the probability distribution of data as described in the Materials and methods section. Values are based on 2 experiments with a total of 11 (Col-0) and 21 (*mlo2-5 mlo6-2 mlo12-1* triple mutant) trichomes analyzed. The *P*-value was computed according to Wilcoxon–Mann–Whitney and indicates the statistical difference between the mobility of GFP-PMR4 in the Col-0 WT background and the *mlo2-5 mlo6-2 mlo12-1* background.

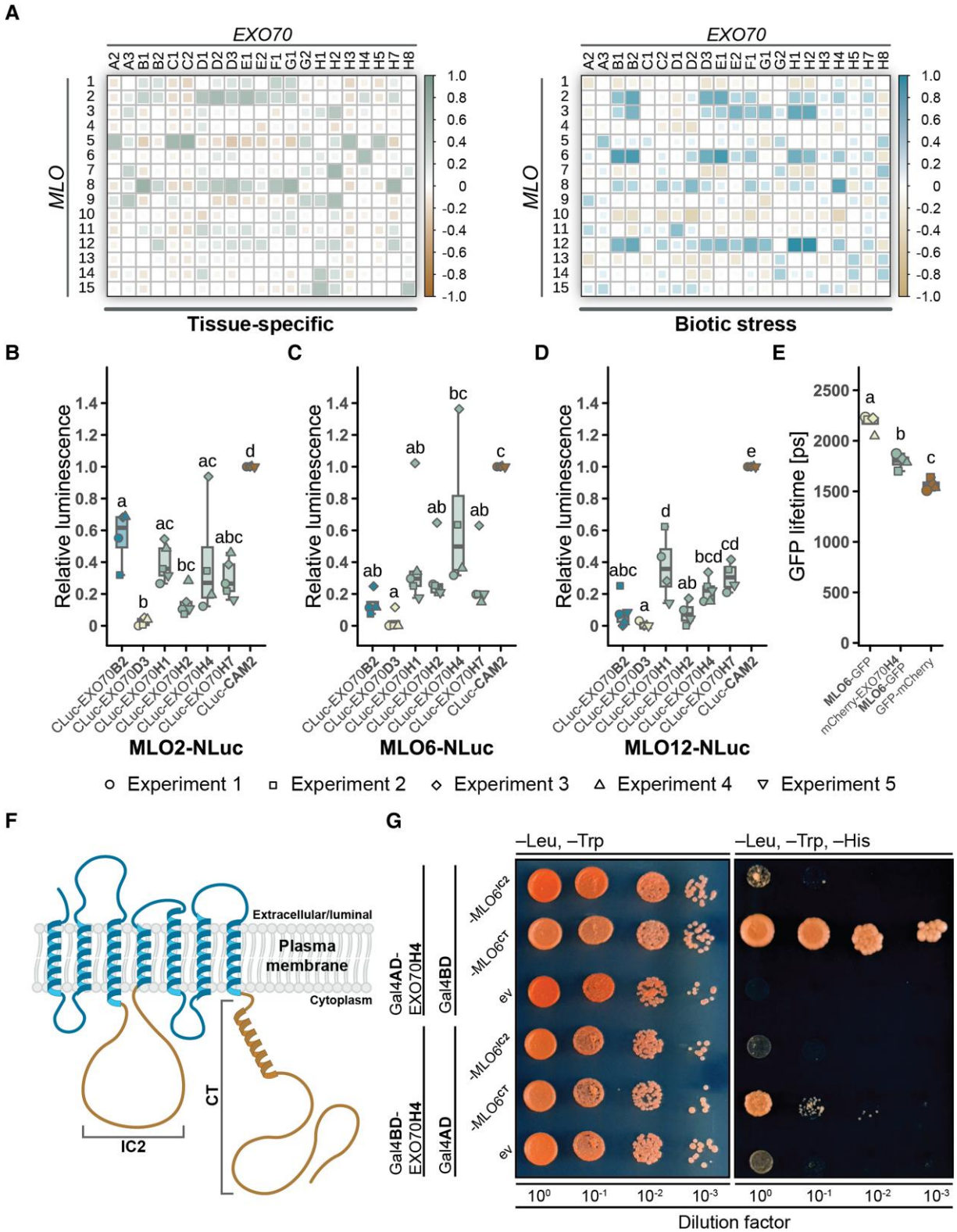

Figure 6. Interaction between clade V MLO proteins and different EXO70 proteins. **A)** Tissue-specific or biotic stress-induced correlation of *MLO* and *EXO70* transcript abundance. Transcript data (note that no data were available for *EXO70A1* and *EXO70H6*) were retrieved from the Arabidopsis eFP browser (http://bar.utoronto.ca/efp/cgi-bin/efpWeb.cgi) on April 19, 2021. Pearson correlation was calculated to assess the co-expression of individual *MLO* and *EXO70* pairs. Squares illustrate Pearson correlation coefficients as indicated by the intensity scales on the right side of each graph. **B to D)** Luciferase complementation imaging of different CLuc-EXO70 and MLO2/6/12-NLuc protein variant combinations was carried out by transient gene expression in *N. benthamiana*. Representative leaves exhibiting luminescence signals detected for the various combinations are shown in

(continued)

exo70H4-1 mutant (Kulich et al. 2018). When we expressed a GFP-tagged version of PMR4 in stably transformed *mlo2-5 mlo6-2 mlo12-1* triple mutant plants, we did not observe the characteristic cell wall localization pattern of the protein that was seen in PMR4-transgenic Col-0 WT plants. Instead, GFP-PMR4-marked endomembrane bodies were more dynamic in the *mlo* triple mutant, as revealed by the imaging of single confocal planes (Fig. 5F). Moreover, time-series imaging and minimal-intensity projection microscopy revealed that the number of clustered immobile GFP-PMR4-labeled endomembrane bodies (speckles), which likely represent PMR4-containing endomembrane compartments formed during exocytosis (Kulich et al. 2018), was significantly lower in the PMR4-transgenic *mlo2-5 mlo6-2 mlo12-1* triple mutant plants than in the respective transgenic Col-0 plants (Fig. 5, F and G). The latter technique enabled us to discriminate mobile from stationary structures in time-lapse series. These data indicate that the delivery of PMR4 to the PM and, thus, ultimately to the secondary cell wall, is perturbed in the *mlo* triple mutant, as previously observed for the *exo70H4-1* mutant (Kulich et al. 2018).

Clade V MLO proteins interact with different EXO70 proteins in an isoform-preferential manner

Based on the similar phenotypic aberrations of rosette leaf trichomes in the *exo70H4-1* mutant and *mlo2 mlo6 mlo12* triple mutants (Figs. 1 and 2) and the colocalization of EXO70H4 and MLO proteins in trichomes (Fig. 5, A and B), we hypothesized that EXO70H4 and MLO2, MLO6, and MLO12 might not only be active in the same cellular pathway but also may physically interact. Furthermore, we speculated that such an interaction would not inevitably be confined to EXO70H4 but may also involve other EXO70 isoforms. As gene co-expression can serve as an indicator of co-functionality in a particular process (Humphry et al. 2010; Gupta and Pereira 2019), we took advantage of published transcript data (Winter et al. 2007) to identify potential candidate EXO70 proteins for an interaction screening with MLO proteins (Fig. 6).

Using tissue-specific or biotic stress-associated data sets, we carried out a co-expression analysis and calculated Pearson correlation coefficients (ρ) for all combinations of *MLO* and *EXO70* genes in *A. thaliana* (Fig. 6A note that no transcript data were available for *EXO70A1* and *-H6*). We placed particular emphasis on *EXO70* genes that showed a high and positive correlation with genes encoding clade V MLO proteins (MLO2, MLO6, and MLO12). With regards to tissue-specific data, we found that *MLO2* expression was correlated with *EXO70D2* ($\rho = 0.63$) and *EXO70E1* ($\rho = 0.62$; Fig. 6A, Tissue-specific). Strikingly, *MLO6* showed a high correlation with *EXO70H4* ($\rho = 0.63$), consistent with the notion that both genes were found to be strongly expressed in trichomes. Moreover, in this cell type, *EXO70H4* showed the highest transcript abundance of all *EXO70* paralogs (Marks et al. 2009; Gilding and Marks 2010) and is the eleventh most highly expressed gene in mature trichomes, as compared to rosette leaves with trichomes removed (Jakoby et al. 2008). Similarly, in trichomes, *MLO6* exhibited the highest trichome transcript levels of all 15 *MLO* paralogs, followed by *MLO2* (Marks et al. 2009). Concerning biotic stress-associated expression, *MLO2*, *MLO6*, and *MLO12* but also the closely related *MLO3* displayed strongly correlated expression with the *EXO70* genes *-B1* and *-B2*, *-D3*, *-E1* and *-E2*, *-F1* as well as *-H1* and *-H2* (Fig. 6A, Biotic stress). In particular, the expression of *EXO70H1* and *EXO70H2* showed a high level of correlation with *MLO12* ($\rho = 0.93$).

Based on these co-expression data, we carried out an initial screening of MLO6–EXO70 interaction by in planta luciferase complementation imaging (LCI) assays following transient co-expression of the candidate genes with the p19 silencing suppressor in leaves of *Nicotiana benthamiana* (Supplementary Fig. S6A). In this experiment, amino- (NLuc) and carboxy-terminal (CLuc) fragments of firefly luciferase were fused with the proteins of interest, leading to restored luciferase activity (and consequently enhanced luminescence) upon direct or indirect interaction of the 2 proteins (Chen et al. 2008). We used the established interaction between MLO

Figure 6. (Continued)
Supplementary Fig. S7A. For normalization, luminescence signals were divided by the signal obtained for the interaction of MLO-NLuc with CLuc-CAM2 (*A. thaliana* CALMODULIN 2; positive control) on the same leaf. The in planta production of recombinant proteins tagged with NLuc or CLuc was assessed by immunoblotting (Supplementary Fig. S7B). Box plots represent the probability distribution of data as described in the Materials and methods section. Values are based on at least 4 independent experiments while individual data points represent the mean of 2 technical replicates each. Letters assign differences of statistical significance (pairwise Student's *t*-test corrected by FDR, $\alpha = 0.01$). **E)** FRET-FLIM analysis of the interaction of mCherry-EXO70H4 with MLO6-GFP was performed by transient gene expression of constructs in *N. benthamiana* and determination of donor (GFP) fluorescence lifetimes. MLO6-GFP was used as a negative control, and GFP-mCherry as a positive control. Box plots represent the probability distribution of data as described in the Materials and methods section. Values shown were derived from 4 independent experiments with 3 cells and 5 regions of interest per cell analyzed. Letters assign differences of statistical significance (pairwise Wilcoxon–Mann–Whitney test corrected by FDR, $\alpha = 0.05$). **F)** Generic membrane topology of a clade V MLO protein. Protein domains that were subject to yeast two-hybrid analysis are shaded in brown. IC2, second intracellular loop; CT, carboxy terminus. **G)** Yeast two-hybrid experiment to test the interaction of EXO70H4 with $MLO6^{IC2}$ or $MLO6^{CT}$. *S. cerevisiae* cultures expressing recombinant *EXO70H4* and *MLO6* constructs were spotted on a medium deprived of (i) leucine (−Leu) and tryptophan (−Trp) or (ii) leucine, tryptophan, and histidine (−His) in 4 different serial 1:10 dilutions. The images are representative of the outcome of 3 independent experiments (Supplementary Fig. S8A). The production of recombinant yeast bait and prey proteins was validated by immunoblotting (Supplementary Fig. S8B). AD, activation domain; BD, binding domain; ev, empty vector.

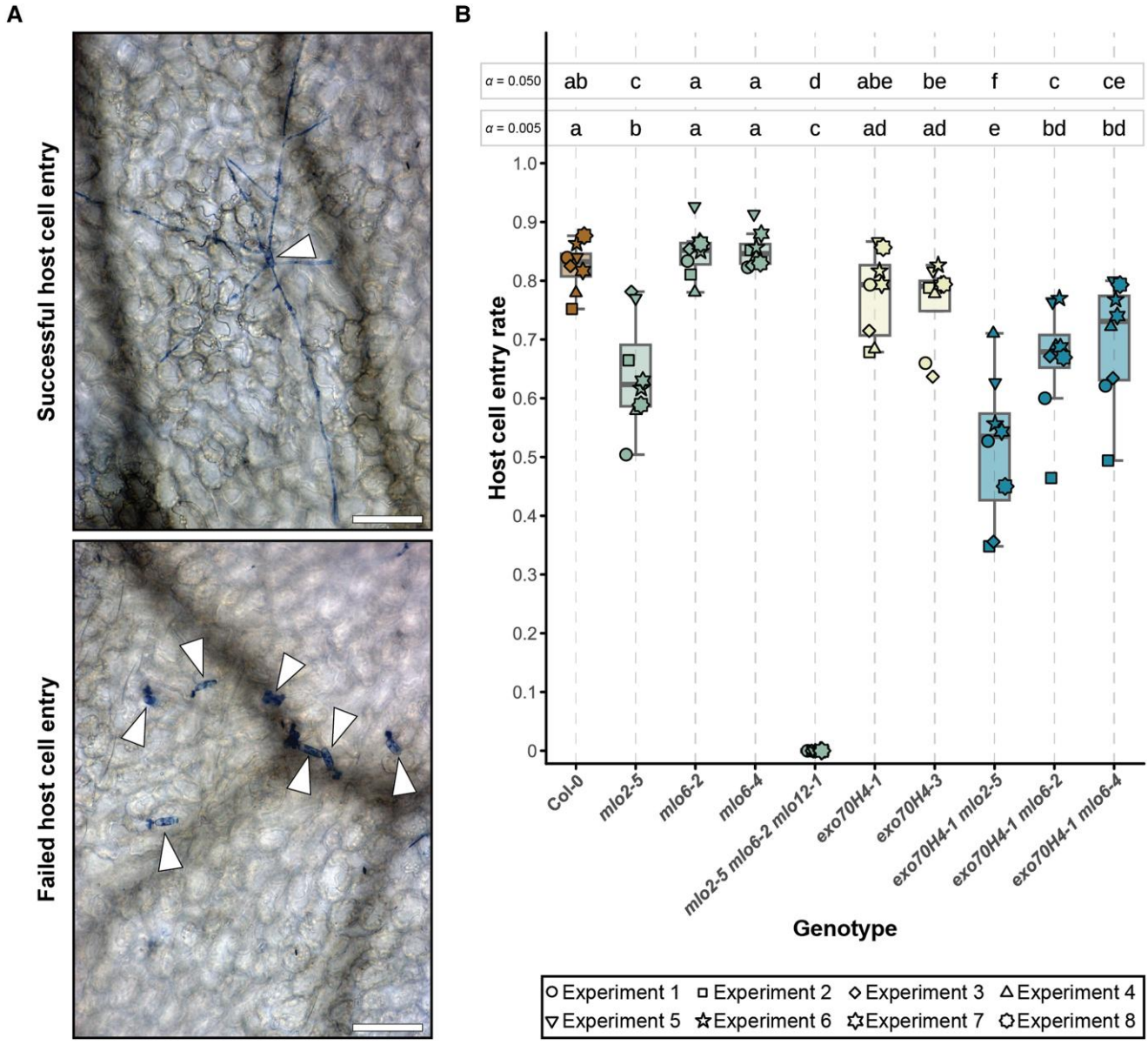

Figure 7. Host cell entry by *E. cruciferarum* is reduced on *exo70H4 mlo* double mutant lines. **A)** Successful and unsuccessful penetration of *E. cruciferarum* conidiospores (arrowheads) on rosette leaves of *A. thaliana*. The presence of secondary hyphae at 72 h post-inoculation reveals successful host cell entry (top) whereas appressorium formation without the development of secondary hyphae indicates unsuccessful host cell entry (bottom). Fungal structures were stained with Coomassie Brilliant Blue. Scale bars represent 100 μm. **B)** Rates of host cell entry of *E. cruciferarum* into rosette leaves of various *A. thaliana* genotypes at 72 h post-inoculation. Box plots represent the probability distribution of data as described in the Materials and methods section. Values are based on 8 independent experiments (see key at bottom), and the individual data points represent the arithmetic mean of data from 3 plants each. Two rosette leaves were assessed per plant, and ~50 fungal attack sites were scored per rosette leaf, i.e. ~2,400 sites per genotype in total. Letters assign differences of statistical significance (pairwise Student's *t*-test corrected by FDR, $\alpha = 0.05$ or 0.005 as indicated on top of the box plot).

proteins and the cytosolic calcium sensor calmodulin (Kim et al. 2002) as a positive control in this set of experiments. In the initial screening, we found a significantly enhanced (>0.24) relative luminescence (in relation to the calmodulin positive control) for the combination of MLO6 (carboxyl-terminally tagged with NLuc) with members of the EXO70H family (amino-terminally tagged with CLuc) in comparison to most of the other EXO70 proteins tested (Supplementary Fig. S6A). We, therefore, selected EXO70H1 (At3g55150), EXO70H2 (At2g39380), EXO70H4, and EXO70H7 (At5g59730) for subsequent comprehensive analysis of protein–protein interactions including, apart from MLO6, also MLO2, and MLO12. Furthermore, we also involved EXO70B2 (At1g07000) and EXO70D3 (At3g14090) as controls because these 2 CLuc-tagged proteins showed low luminescence values (<0.07) in combination with MLO6-NLuc

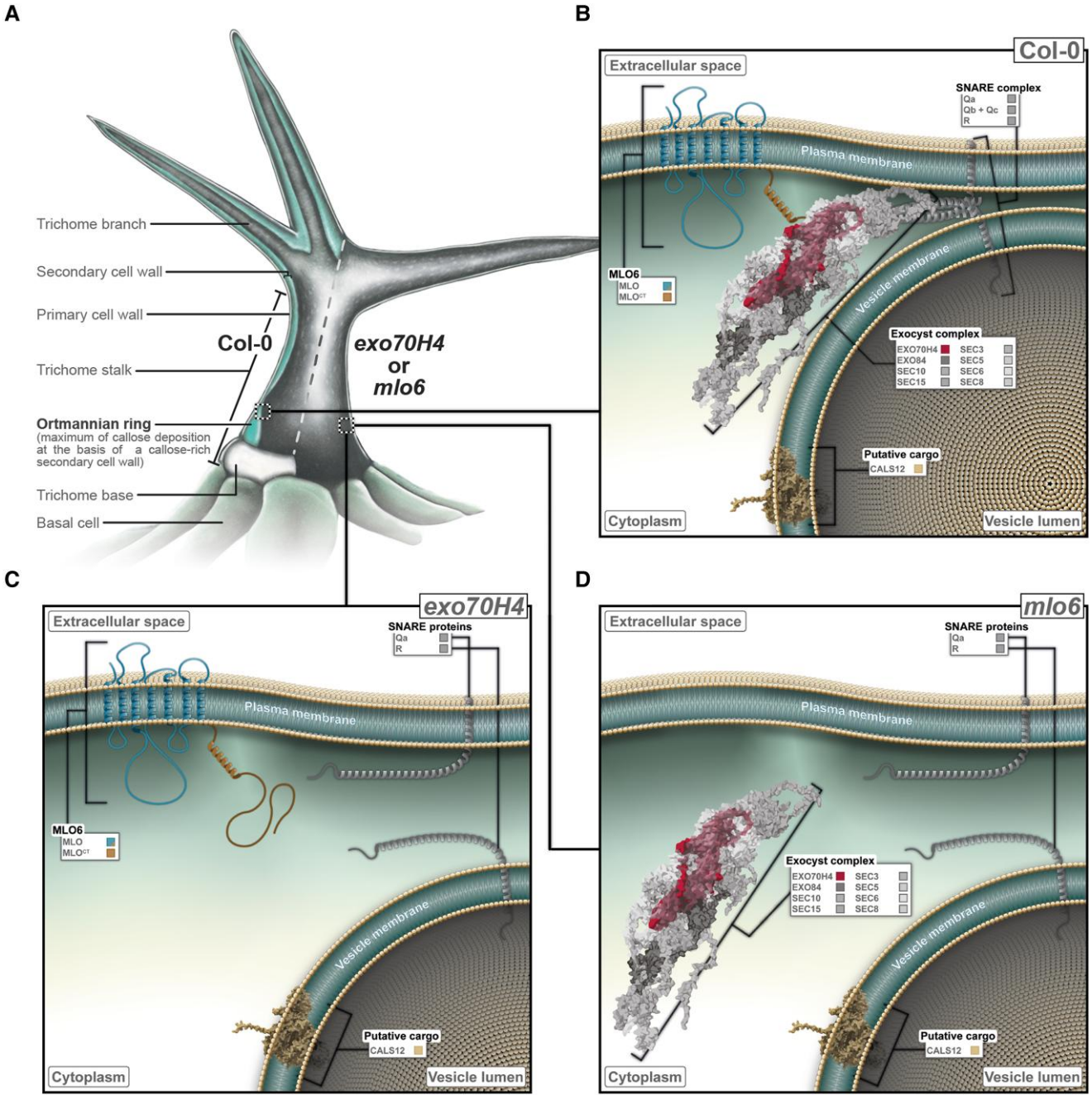

Figure 8. Models showing how EXO70H4 and MLO6 jointly confer the deposition of callose in the secondary cell walls of rosette leaf trichomes. **A)** Schematic depiction of an *A. thaliana* rosette leaf trichome of a Col-0 WT plant (left half of the trichome, separated by a dashed line) and on an *exo70H4* or *mlo6* mutant plant (right half of the trichome). Col-0 WT trichomes accumulate the cell wall polymer callose in their secondary cell walls. The deposition of callose in the secondary cell wall of WT trichomes is most pronounced in the medial stalk region, forming the OR. The cell wall domain at the trichome base is callose-free. Trichomes on *exo70H4* and *mlo6* mutant plants exhibit no or an erratic (not shown) deposition of callose. **B)** Illustration of EXO70H4–MLO6-guided localized secretion in Col-0 WT trichomes. Secretory vesicles that contain the CALS12 callose synthase as putative cargo are recruited to distinct sites of the cellular cortex by the interaction of MLO6 with EXO70H4, resulting in SNARE complex-dependent vesicle fusion and exocytosis. The interaction of MLO6 and EXO70H4 is mediated by the intracellular MLO C-terminus (MLO^{CT}). Note that proteins toned in gray were not a subject of experiments carried out in this study. **C, D)** The localized secretion of CALS12 is impaired in *exo70H4* (C) and *mlo6* (D) mutant trichomes, leading to either no or erratic (not shown) deposition of callose in the trichome secondary cell walls.

(Supplementary Fig. S6A), despite their evident accumulation in transformed *N. benthamiana* tissue (Supplementary Fig. S6B).

For MLO2-NLuc, we observed significantly enhanced relative luminescence after co-expression with CLuc-EXO70H1 (arithmetic mean ~0.39) and -H4 (~0.40) as opposed to

CLuc-EXO70D3 (~0.02; Fig. 6B and Supplementary Fig. S7A). Strikingly, the combination of MLO2-NLuc and CLuc-EXO70B2 generated a signal with an average relative luminescence intensity of ~0.56. This strong signal contrasts the values obtained with the MLO6-NLuc/CLuc-EXO70B2 (~0.14) and MLO12-NLuc/CLuc-EXO70B2 (~0.10) combinations (Fig. 6, C and D), and it suggests a preferred interaction of MLO2 with EXO70B2. In the case of MLO6-NLuc, the strongest relative luminescence was observed upon co-expression with CLuc-EXO70H4 (~0.67; Fig. 6C, Supplementary Fig. S7, A and B), whereas MLO12-NLuc showed enhanced relative luminescence in combination with CLuc-EXO70H1 (~0.37; Fig. 6D, and Supplementary Fig. S7, A and B).

To further validate the interaction between EXO70H4 and MLO6, we performed in planta Förster resonance energy transfer (FRET) analysis, which we conducted by donor fluorescence lifetime imaging (FLIM). The FRET-FLIM method, which is considered the gold standard for FRET analysis of protein–protein interactions (Lalonde et al. 2008), determines the decrease in donor fluorescence lifetime when an acceptor fluorophore is close enough (typically <10 nm) for FRET to occur, indicating the intimate association of the 2 fluorophore-tagged proteins (Bastiaens and Squire 1999; van Leeuwen et al. 2007; Martin et al. 2018). In our experiments, we used MLO6-GFP as the donor and mCherry-EXO70H4 as the acceptor molecule. The GFP-mCherry fluorophore pair has been suggested to be well-suited for effective FRET-FLIM measurements in living cells (Albertazzi et al. 2009). MLO6-GFP (donor alone) was used as a negative control, and a GFP-mCherry fusion protein designed for intramolecular FRET served as the positive control. All constructs were driven by the constitutive cauliflower mosaic virus *35S* promoter (*ProCaMV35S*) and were transiently co-expressed with the p19 silencing suppressor in *N. benthamiana* leaves upon agroinfiltration (Supplementary Fig. S7C). Expression of the MLO6-GFP negative control yielded a mean donor fluorescence lifetime of ~2.18 ns (Fig. 6E), comparable to the result using EGFP alone, as described previously (Martin et al. 2018). The positive control (GFP-mCherry) exhibited a strongly reduced donor fluorescence lifetime (~1.56 ns), as expected. Co-expression of MLO6-GFP (donor) and mCherry-EXO70H4 (acceptor) resulted in an intermediate donor fluorescence lifetime of ~1.80 ns, which was significantly different from both the positive and the negative control according to statistical testing (Fig. 6E). The reduction in donor fluorescence lifetime is strongly indicative of an interaction between the fluorophore-tagged EXO70H4 and MLO6 proteins.

As both LCI (Fig. 6, B to D) and FRET-FLIM (Fig. 6E) experiments pointed to a direct interaction of particular EXO70.2 proteins with specific clade V MLO proteins, we aimed to characterize this interplay further by delimiting the interacting region within the MLO protein. For this purpose, we focused on the strong MLO6–EXO70H4 interaction (Fig. 6C) and reasoned that the second intracellular loop (IC2) and the carboxyl terminus (CT), comprising the largest cytoplasmic regions of MLO proteins (Devoto et al. 1999; Fig. 6F), would be the regions of the protein most likely involved in the interaction with EXO70H4. We carried out yeast two-hybrid assays and tested EXO70H4 as a bait protein with both $MLO6^{IC2}$ and $MLO6^{CT}$ as prey proteins (Fig. 6F). On selective media lacking histidine, we observed growth of yeast colonies harboring the EXO70H4/$MLO6^{CT}$, but not the EXO70H4/$MLO6^{IC2}$, combination, indicating an interaction between EXO70H4 and the MLO6 carboxy terminus (Fig. 6G and Supplementary Fig. S8A), although bait and prey proteins were detectable in all cases (Supplementary Fig. S8B). By contrast, but reminiscent of the LCI data (Fig. 6C), EXO70D3 failed to interact with both $MLO6^{IC2}$ and $MLO6^{CT}$ (Supplementary Fig. S8C), in spite of its marked accumulation as a bait protein (Supplementary Fig. S8D).

Exo70 mlo mutants show increased resistance to entry of the powdery mildew pathogen into host cells

As various types of cell wall analyses and protein–protein interaction experiments indicated an interplay of EXO70H4 and MLO clade V proteins, we wondered if plants deprived of EXO70H4, alone or in combination with mutations in *MLO* genes, would exhibit an altered infection phenotype upon challenge with an adapted powdery mildew pathogen. Thus, we inoculated *exo70H4* and *mlo* mutant plants as well as a selection of combined *exo70H4 mlo* mutants with conidiospores of *Erysiphe cruciferarum* and scored fungal host cell entry success on these genotypes (Fig. 7A). Consistent with previous studies (Consonni et al. 2006; Consonni et al. 2010), we observed that ~82% (arithmetic mean) of fungal sporelings successfully penetrated leaf epidermal cells of Col-0 WT plants at 72 h after inoculation (Fig. 7B). Likewise, we scored WT-like levels of fungal host cell entry on *mlo6-2* (~85%) and *mlo6-4* (~85%) single mutants. Unlike *mlo6* plants, *mlo2-5* (~64%) mutants supported significantly lower levels of host cell entry compared to Col-0, while *mlo2-5 mlo6-2 mlo12-1* triple mutants were completely resistant (~0%) as described before (Consonni et al. 2006; Acevedo-Garcia et al. 2017).

For *exo70H4* single mutants, we observed lower levels of penetration on *exo70H4-1* (~78%) and *exo70H4-3* (~76%) lines compared to Col-0 (~82%—see above), pointing toward a slightly enhanced resistance phenotype of these mutants. Two different allele combinations of combined *exo70H4 mlo6* mutants, however, allowed significantly less fungal penetration (*exo70H4-1 mlo6-2* ~66%, *exo70H4-1 mlo6-4* ~70%) than Col-0 WT plants and *mlo6* single mutant lines (~85%—see above), and tended to allow less host cell entry than did the corresponding *exo70H4-1* single mutant line (~78%). Similarly, *exo70H4-1 mlo2-5* double mutants were significantly less susceptible (~51%) than Col-0 plants (~82%), and the partly resistant *mlo2-5* (~64%) and *exo70H4-1* (~78%) single mutant lines (Fig. 7B). Taken together, these data indicate both an additive reduction of the rate of entry of *E. cruciferarum* into host cells in the *exo70H4-1 mlo2-5* double mutant in comparison to the respective single mutants and a synergistic reduction of fungal

entry success in the 2 *exo70H4-1 mlo6* double mutants compared to the corresponding single mutants (Supplementary Fig. S9).

Fluorophore-tagged EXO70H4 accumulates weakly at sites of attempted pathogen entry

Several types of defense-related proteins have been previously shown to accumulate in and around cell wall appositions formed beneath powdery mildew appressoria at attempted pathogen entry sites (Assaad et al. 2004; Bhat et al. 2005; Stein et al. 2006; Kwon et al. 2008a; Meyer et al. 2009; Ortmannová et al. 2022). We aimed to explore whether this would be also the case for EXO70H4. We initially focused on MLO2 and the SNARE protein SYP121 (PEN1), which both play a key role in the plant-powdery mildew interaction (Collins et al. 2003; Consonni et al. 2006), as presumed positive controls. Transgenic *A. thaliana* lines expressing fluorophore-tagged versions of these 2 proteins under the control of the constitutive *CaMV35S* promoter in the respective *pen1-1* or *mlo2-6 mlo6-4 mlo12-8* mutant background revealed frequent and obvious focal accumulation of GFP-SYP121 and MLO2-YFP at *E. cruciferarum* attack sites (Supplementary Fig. S10), as expected (Assaad et al. 2004; Bhat et al. 2005; Meyer et al. 2009). By contrast, the outcome was weaker and more variable in the case of EXO70H4. Transgenic lines expressing fluorophore-tagged EXO70H4 versions under the control of either the endogenous (*ProEXO70H4*) or a constitutively active (*ProUBIQUITIN10*) promoter showed signs of EXO70H4 protein accumulation at powdery mildew attack sites only in some instances. Moreover, EXO70H4 protein accumulation was weaker and less confined than in the case of SYP121 and, in particular, MLO2 (Supplementary Fig. S10).

exo70H4 and *mlo* mutants are not evidently impaired in the accumulation of callose at sites of attempted pathogen entry

Apart from defense-related proteins, the carbohydrate polymer callose accumulates in localized cell wall appositions (papillae) formed in response to attempted powdery mildew ingress. The formation of this papillary callose relies on the callose synthase PMR4 (GSL5/CALS12; Jacobs et al. 2003; Nishimura et al. 2003), which is a known cargo of EXO70H4-mediated exocytosis (Kulich et al. 2018). To study whether localized callose deposition in response to pathogen attack would be impaired by the absence of EXO70H4 or MLO proteins, we studied this aspect in a set of *A. thaliana* mutants. *E. cruciferarum*-inoculated leaf specimens were harvested at 48 hpi, stained with aniline blue, and subjected to confocal laser scanning microscopy. We observed the frequent, yet variable, presence of callose deposits beneath attempted fungal entry sites in the case of Col-0 WT plants. By contrast, *pmr4-1* mutant plants showed little, if any, accumulation of papillary callose, as expected (Jacobs et al. 2003; Nishimura et al. 2003). Similar to Col-0 WT plants, all other genotypes tested (*exo70H4-1*, *exo70H4-3*, *mlo2-5*, and *mlo6-2* single mutants, *exo70H4-1 mlo2-5*, *exo70H4-1 mlo6-2*, and *exo70H4-1 mlo6-4* double mutants as well as the *mlo2-5 mlo6-2 mlo12-1* triple mutant) showed frequent, yet variable, callose deposition at attempted fungal entry sites (Supplementary Fig. S11). We conclude that mutations in *EXO70H4* and *MLO2* or *MLO6*, alone or in combination, do not discernibly affect the delivery of callose in powdery mildew-triggered cell wall appositions.

Discussion

We discovered a functional interplay between EXO70H4 and MLO2, MLO6, and MLO12 in the context of cell wall-related secretory processes in trichomes of *A. thaliana* rosette leaves. We propose that MLO–EXO70H4 pairs (in particular EXO70H4 and MLO6) jointly recruit the exocyst complex to distinct domains of the cell cortex of trichomes, promoting the localized secretion of cargos such as the CALS12 callose synthase (Fig. 8). This claim rests on (i) a marked phenotypic overlap of *exo70H4* and *mlo2 mlo6 mlo12* triple mutants regarding secretion-dependent trichome secondary cell wall features (Figs. 1, 2, and 3), (ii) differences in trichome cell wall composition in *exo70H4* and *mlo2 mlo6 mlo12* triple mutant plants as revealed by biochemical analysis and/or FTIR spectroscopy of isolated trichomes (Fig. 4), (iii) extensive colocalization of fluorophore-labeled EXO70H4 and MLO2, MLO6, and MLO12 proteins (Fig. 5A), (iv) mislocalization of fluorophore-tagged EXO70H4 in *mlo2 mlo6 mlo12* triple mutant plants (Fig. 5B) and MLO6-GFP in the *exo70H4* mutant (Fig. 5C), (v) shared enhanced mobility of GFP-PMR4-marked intracellular compartments in transgenic *exo70H4* and *mlo2 mlo6 mlo12* mutant lines (Fig. 5, D and E; Kulich et al. 2018), (vi) isoform-preferential interaction between EXO70 and MLO proteins (Fig. 6), and (vii) synergistically enhanced powdery mildew resistance in *exo70H4 mlo6* double mutants (Fig. 7). Taken together, this comprehensive data set leads to the intriguing conclusion that EXO70 and MLO proteins are involved in the same cellular pathway or may even reside within the same macromolecular complex. Indeed, both EXO70 subunits and MLO proteins have been implicated in localized secretion (Heider and Munson 2012; Meng et al. 2020; Žárský et al. 2020), suggesting that this process is the common denominator and, therefore, is likewise affected in *exo70* as well as *mlo* mutants.

While the exocyst has a well-established function in secretory processes, the role of MLO proteins therein remains enigmatic. MLO proteins were recently demonstrated to function as PM-localized calcium channels (Gao et al. 2022). Calcium influx is a proven trigger for exocytosis in eukaryotic cells, promoting vesicle fusion events at the PM (Barclay et al. 2005). Established examples of calcium-induced secretion in mammals are synaptic vesicle exocytosis in neurons, granule exocytosis in mast cells, and hormone exocytosis in endocrine cells. Mechanistically, the calcium signal is transmitted via cytoplasmic calcium sensors to the membrane fusion

machinery, of which synaptotagmins are arguably the best-studied ones (Pang and Südhof 2010). In *A. thaliana*, synaptotagmin 5 was recently suggested to regulate secretory immune responses mediated by the SYP132–VAMP721/722 SNARE protein module (Kim et al. 2021). We hypothesize that PM-localized MLO calcium channels permit calcium influx-dependent and possibly spatially confined secretory events, which also involve the physical association of MLO proteins with EXO70 proteins. The protein–protein interaction between a member of the exocyst complex and an MLO calcium channel might determine the actual site of vesicle fusion events, thereby allowing for precisely fine-tuned polar exocytosis. This scenario is compatible with absent or erratic exocytosis in *exo70* and *mlo* mutant plants (Fig. 8, A, C, and D), resulting in stochastic patterns of secondary cell wall biogenesis in trichomes, as observed in our experiments (Figs. 1 to 3). The shared phenotype of *exo70H4* and *mlo* triple mutants reinforces the notion that the interaction between EXO70 and MLO proteins in planta (Fig. 6) is biologically relevant.

If this scenario were true, one may wonder what could be the cargo of the secretory pathway linked to an EXO70H4–MLO regulatory module in trichomes. A prime candidate is the PMR4 (CALS12) callose synthase, which along with CALS9, was shown to be mislocalized in the *exo70H4-1* mutant (Kulich et al. 2018). Likewise, we also observed a similar mislocalization pattern in the *mlo2-5 mlo6-2 mlo12-1* triple mutant (Fig. 5, F and G). This mislocalization of PMR4 is characterized by a reduction of immobile PM-associated GFP-PMR4 speckles and a concomitant increase in mobile GFP-PMR4-labelled membrane bodies, pointing to a reduction of PMR4 secretion in *exo70* and *mlo* triple mutants. Additional cargos of the proposed EXO70H4–MLO secretory pathway that would account for the autofluorescence (possibly conditioned by phenolic compounds; Kulich et al. 2018), the ROS accumulation and heavy metal deposition in trichomes are still unknown. These features were previously found to depend on EXO70H4 ((Kulich et al. 2018) and Kubátová, personal communication). One can, however, speculate about their nature as being related to the detoxification of heavy metals by their deposition in trichomes, as suggested previously (Kulich et al. 2015). For example, the zinc ZIP transporters are highly expressed in trichomes (Jakoby et al. 2008), and a copper transporter (COPT5, At5g20650) was found to be the most enriched protein in a comprehensive trichome proteome analysis (Huebbers et al. 2022). Recent studies reported that copper accumulates at the basal part of the trichome (Kulich et al. 2015; Ricachenevsky et al. 2021), roughly corresponding to the region of the OR. Therefore, copper, and other heavy metal transporters can be considered additional candidates for the EXO70H4–MLO secretory pathway. *A. thaliana* trichomes contain 2 distinct PM domains, with EXO70H4 and specific phospholipids being enriched in the apical one (Kubátová et al. 2019). We, thus, believe that the basal localization of copper in trichomes as described before (Kulich et al. 2015; Ricachenevsky et al. 2021) represents part of the basal domain defined by the absence of EXO70H4 and the presence of EXO70A1 (Kulich et al. 2018; Kubátová et al. 2019). Our heavy metal staining experiments as well as EXO70H4 localization data further support this notion.

While EXO70H4 is involved in all the aspects of trichome cell wall maturation considered in the present study, the contribution of the 3 MLO proteins seems to vary. Previous studies already indicated isoform-specificity for *mlo*-conditioned mutant phenotypes. For example, *A. thaliana* genes *MLO2*, *MLO6*, and *MLO12* confer susceptibility to powdery mildew fungi (Consonni et al. 2006). In the context of this phenotype, the 3 genes exhibit unequal redundancy, with *MLO2* being the major player, resulting in vastly different outcomes for *mlo2* single mutants (partial resistance) and *mlo2 mlo6 mlo12* triple mutants (full resistance; (Consonni et al. 2006)). Similarly, enhanced tolerance to ozone is specifically conditioned by loss-of-function *mlo2* mutants and is further increased in a *mlo2 mlo6 mlo12* triple mutant (Cui et al. 2018). By contrast, both *mlo2* single mutants and *mlo2 mlo6 mlo12* triple mutants show a complete loss of systemic acquired resistance, albeit *MLO6* may have a supportive but less critical role in this type of plant defense (Gruner et al. 2018).

Based on respective mutant phenotypes, we found a major contribution of *MLO6* regarding trichome callose deposition (Supplementary Fig. S1A) and cell wall thickness (Supplementary Fig. S1B) as well as a possible joint function for *MLO2* and *MLO6* regarding trichome cell wall autofluorescence (Supplementary Fig. S1D) and the deposition of heavy metals (Supplementary Fig. S1E). The predominant role of *MLO6* in trichome-associated processes was consistent with the high level of expression of this gene in trichomes (highest expression level of all *MLO* paralogs in this cell type; (Marks et al. 2009)) and the favored interaction of MLO6 with EXO70H4, which is likewise encoded by a gene that is preferentially expressed in trichomes (Fig. 6A; Jakoby et al. 2008). We, thus, assume that the interplay of EXO70H4 and MLO6 is the main driver of localized callose deposition in trichomes (Fig. 8B). However, at least for some of the trichome phenotypes, e.g. altered callose deposition (Supplementary Fig. S1A) and ROS accumulation (Supplementary Fig. S1C), it seems as if the severity of the phenotype in the *mlo* triple mutants exceeds that of the *mlo6* single and/or *mlo2 mlo6* double mutants, suggesting that also MLO12 contributes to these features. Thus, all 3 *MLO* genes appear to add to the various trichome phenotypes to different degrees and with varying redundancy. In summary, the current findings further support the notion of joint, yet unequal, contributions of multiple MLO paralogs to certain biological processes.

Regarding some of the trichome phenotypes, we noticed a weaker penetrance for the *mlo2-6 mlo6-4 mlo12-8* triple mutant as compared to the *mlo2-5 mlo6-2 mlo12-1* triple mutant. This applies to cell wall thickness (Fig. 1E), ROS accumulation (Fig. 2B), and heavy metal deposition

(Fig. 2D) in leaf-attached trichomes as well as the histochemical staining patterns for calcofluor white (Fig. 3A), ruthenium red (Fig. 3B), and toluidine blue O (Fig. 3C) in detached trichomes. The lower penetrance was further revealed regarding global cell wall composition as assessed by FTIR spectroscopy analysis (Fig. 4D) and the levels of the monosaccharides arabinose (Fig. 4A) and galactose (Fig. 4B). A weaker phenotype has been already previously described for the *mlo2-6 mlo6-4 mlo12-8* triple mutant regarding powdery mildew resistance, exemplified by some residual susceptibility to the fungal pathogen (Acevedo-Garcia et al. 2017), which differs from the complete resistance of the *mlo2-5 mlo6-2 mlo12-1* triple mutant (Consonni et al. 2006). The differential outcome of the 2 *mlo* triple mutants in powdery mildew pathogenicity assays has been ascribed to the rather distal insertion site of the T-DNA in the *mlo6-4* allele, possibly resulting in some residual MLO6 function in the context of this mutant and, accordingly, also in the *mlo2-6 mlo6-4 mlo12-8* triple mutant (Acevedo-Garcia et al. 2017). It is, thus, tempting to speculate that trichome phenotypes with a differential manifestation for the 2 *mlo* triple mutants are mainly caused by a loss-of-function of *MLO6*. This notion is further supported by the fact that an independent CRISPR/Cas9-derived *mlo6* null mutant allele (*mlo6-6*) showed a similar phenotype as did the *mlo6-2* single mutant (Supplementary Fig. S2).

Our studies demonstrated physical interactions between EXO70.2 subfamily members and MLO proteins in 3 different in vivo experimental systems: in planta LCI and FRET-FLIM assays as well as yeast two-hybrid assays (Fig. 6, B to E and G, Supplementary Figs. S6 to S8). The LCI experiments revealed preferential interaction of particular EXO70.2 subfamily members and MLO isoforms, yet often also indicated weaker interactions with the non-preferred paralogs. This outcome may point toward some level of promiscuity regarding EXO70–MLO interactions, which may at least in part explain the genetic redundancies observed for some *exo70* and *mlo* mutant phenotypes. The yeast two-hybrid assay delimited the interacting region of MLO6 to its carboxy-terminal cytoplasmic domain (Fig. 6F and Supplementary Fig. S8), which also harbors the conserved calmodulin-binding domain (Kim et al. 2002; Kusch et al. 2016). This section of MLO proteins was recently shown to serve as a regulatory center, modifying the calcium channel activity of MLO proteins in a calcium/calmodulin-dependent autoinhibitory manner (Gao et al. 2022). It will be interesting to study in the future whether the binding of calmodulin to MLO proteins also affects its interaction with EXO70 proteins. It will be likewise informative to dissect EXO70 proteins to find out which parts of these polypeptides associate with MLO proteins.

Our pathogenicity assays revealed a cumulative contribution of *exo70H4* and *mlo2* mutants regarding powdery mildew resistance. While single mutants of these 2 genes showed a moderate decrease in susceptibility (host cell entry) to the fungal pathogen, an *exo70H4 mlo2* double mutant exhibited an additive reduction in host cell penetration (Fig. 7B and Supplementary Fig. S9). Notably, we observed a more than additive (i.e. a synergistic) effect for the 2 *exo70H4 mlo6* double mutants tested (Fig. 7B and Supplementary Fig. S9). The latter outcome is even more surprising, as *mlo6* single mutants did not exhibit any reduction in the rate of entry of the powdery mildew pathogen into host cells (Fig. 7B; Consonni et al. 2006). However, in combination with *mlo2* mutants, *mlo6* (and also *mlo12*) mutations enhanced the *mlo2* pathogen phenotype, indicating unequal genetic redundancy of *MLO2*, *MLO6*, and *MLO12* regarding the modulation of powdery mildew susceptibility (Consonni et al. 2006). Reminiscent of this scenario, a similar cryptic contribution of the *mlo6* mutation becomes apparent in combination with the *exo70H4-1* mutant (Fig. 7B). This result is in line with data from our co-expression analysis (Fig. 6A), trichome phenotypes (Supplementary Fig. S1), and protein–protein interaction experiments (Fig. 6C), indicating a joint expression, mutual interplay and preferred interaction of EXO70H4 and MLO6 in polar exocytosis. In summary, these data reveal a weak yet reproducible role for EXO70H4 in susceptibility to an adapted powdery mildew pathogen. We hypothesize that, similar to MLO2, MLO6, and MLO12, additional EXO70 paralogs may contribute redundantly to this process. This notion is supported by the expression profiles of *EXO70* genes upon biotic stresses (Fig. 6A), which identified other *EXO70.2* subfamily members as highly expressed under these conditions. Analysis of higher-order *exo70* mutants, with or without additional *mlo* mutations, will be required to elucidate the putative overlapping and/or redundant functions of EXO70 proteins in plant defense against powdery mildew fungi.

We hypothesize that EXO70 and MLO proteins jointly regulate secretory processes in the context of plant immunity, including powdery mildew challenge. Cellular polarization and polar secretion have long been suggested to be decisive in antifungal defense (Schmelzer 2002; Yun et al. 2008; Kwon et al. 2008b). Indeed, genetic studies have identified and characterized components of the secretory machinery, such as SNARE proteins and ATP-binding cassette transporters, as being crucial for effective preinvasive immunity against adapted and non-adapted powdery mildew fungi, including in the context of *mlo*-based resistance (Collins et al. 2003; Consonni et al. 2006; Kwon et al. 2008a; Bednarek et al. 2009). The herein-described identification of EXO70 subunits as additional factors involved in this process further highlights the presumed role of polar secretion in antifungal defense at the cell wall. Deregulated secretory processes in *mlo* and *exo70* mutants may result in a constitutively altered cell wall architecture in these mutants, which might in part account for their altered pathogen infection phenotypes. Further cell wall analyses, in particular in leaf tissue, the primary target of powdery mildew fungi, will be required to substantiate this notion. Nonetheless, recently reported direct interactions of both MLOs and plant exocyst subunits (including EXO70s) with SNARE proteins reinforce

the conclusion that both types of proteins are part of a hierarchical module regulating exocytosis (Larson et al. 2020; Meng et al. 2020; Ortmannová et al. 2022). Although we consider the PMR4 callose synthase as an important cargo of EXO70–MLO cooperation in the context of trichome secondary cell walls, PMR4 is unlikely to play a major role regarding powdery mildew resistance, as a previous study demonstrated that *mlo2*-mediated resistance is independent of PMR4-based callose deposition (Consonni et al. 2010).

An involvement of EXO70 proteins in plant immunity has been described before. For example, *A. thaliana* EXO70B1 and EXO70B2 were previously reported by several studies to be linked to pathogen defense. *exo70b1* mutant plants exhibited altered infection outcomes upon challenge with various pathogens, associated with a lesion-mimic cell death phenotype and reduced responsiveness to microbe-derived molecules (Stegmann et al. 2013; Zhao et al. 2015). The activated defense responses of the *exo70B1* mutant rely on a truncated resistance protein of the NOD-like receptor class (TN2), which might monitor the integrity of EXO70B1 (Zhao et al. 2015). Furthermore, *exo70B2* and *exo70H1* mutants show increased susceptibility to the bacterial pathogen *Pseudomonas syringae* pv. *maculicola* (Pečenková et al. 2011). The *exo70B2* mutant exhibited, in addition, the formation of aberrant local cell wall appositions (papillae) in response to inoculation with the barley powdery mildew pathogen, *B. hordei* (Pečenková et al. 2011; Ortmannová et al. 2022). Finally, both EXO70B1 and EXO70B2 regulate the trafficking of the pattern recognition receptor FLS2, which recognizes bacterial flagellin, to the PM (Wang et al. 2020). Apart from *A. thaliana*, EXO70 proteins have been linked to plant immunity in several other plant species. In barley, for example, EXO70FX12, a member of a lineage-specific EXO70 clade, is required for receptor kinase-mediated disease resistance to the wheat stripe rust pathogen, *Puccinia striiformis* f.sp. *tritici* (Holden et al. 2022). It is, thus, not surprising that defense-related EXO70.2 subunits such as EXO70B1 are targets of pathogen-derived effector molecules that affect their function (Wang et al. 2019; Žárský et al. 2020; Michalopoulou et al. 2022). It will be interesting to study whether effector proteins of powdery mildew fungi target EXO70 subunits and/or MLO proteins for promoting virulence.

While we provide in our work strong support for an EXO70–MLO interplay, we acknowledge that our current data do not offer any evidence for a contribution of the exocyst core subunits to this protein–protein association, although we previously showed in a yeast two-hybrid assay that EXO70H4 does interact with the *A. thaliana* exocyst core subunits SEC5A, SEC6, and EXO84B (Kulich et al. 2015). It, therefore, remains a formal possibility that the newly discovered EXO70–MLO interaction relates to cellular functions other than secretory processes, involving noncanonical EXO70 activities without the entire exocyst complex. However, we consider this scenario rather unlikely given that so far plant EXO70 subunits have been exclusively linked to functions in exocytosis, and because both *exo70H4* and *mlo* mutants exhibit mutant phenotypes in trichomes that are indicative of perturbed secretion (Figs. 1 and 2; Supplementary Fig. S1). Moreover, we have previously observed that in mutants of the *A. thaliana EXO84B* core subunit, overall trichome morphogenesis is compromised (Fendrych et al. 2013), indicating that the exocyst complex is already involved in primary cell wall development in early trichomes. Further work will be required to unravel whether the herein proposed EXO70–MLO module also operates in other biological processes in which EXO70 and MLO proteins have been implicated before (Chen et al. 2009; Kessler et al. 2010; Meng et al. 2020).

Materials and methods

Plant material

The *Arabidopsis thaliana exo70H4-1* (SALK_023593; Kulich et al. 2015) and *exo70H4-3* (SALK_003200; Kulich et al. 2015) mutants, the *mlo2-5 mlo6-2 mlo12-1* (Consonni et al. 2006) and *mlo2-6 mlo6-4 mlo12-8* (Acevedo-Garcia et al. 2017) triple mutants, as well as the respective *mlo* single and double mutants, are T-DNA/transposon insertion mutants in the background of ecotype Col-0 (Supplementary Fig. S2A). In the context of this study, we generated an additional *mlo6* mutant allele (*mlo6-6*) in the Col-0 background by CRISPR-Cas9-mediated gene editing (see below; Supplementary Fig. S2B). The *A. thaliana pmr4-1* (Vogel and Somerville 2000) and *eds1-1* mutants (Falk et al. 1999) are ethyl methansulfonate-induced mutants. The following transgenic lines have been described before: mCherry-EXO70H4 under the control of the native *EXO70H4* promoter in Col-0 WT (Kulich et al. 2018); GFP-PMR4 under the control of the *UBIQUITIN10* promoter in Col-0 WT (Kulich et al. 2018), and GFP-PEN1 under the control of *ProCaMV35S* in the *pen1-1* mutant background (Assaad et al. 2004). Oligonucleotides used for plant genotyping are listed in Supplementary Table S2.

Plant cultivation

A. thaliana and *N. benthamiana* plants were sown on SoMi 531 soil (HAWITA, Vechta, Germany). Seeding and harvest of *A. thaliana* plants that were used for trichome isolation were carried out as described previously (Huebbers et al. 2022). For all experiments, plants were cultivated at 22/20 °C average day/night temperature with a photoperiod of 10/14-h d^{-1} light/darkness, a photosynthetic photon flux density of 80 to 100 μmol m^{-2} s^{-1}, and a relative humidity of 80% to 90%. Before leaf-to-leaf touch inoculation (see section Assessment of entry of *E. cruciferarum* into host cells below for details) with *E. cruciferarum*, 35-d-old *A. thaliana* plants (21-d-old for callose accumulation assays) were placed in a separate growth chamber with the same photoperiod and photosynthetic photon flux density as described above but a constant temperature of 20 °C and a relative humidity of 68%. Photoperiod and photosynthetic photon flux density

were the same as described above. Leaves of inoculated *A. thaliana* plants were sampled at 24 h post-inoculation to investigate the focal accumulation of fluorophore-tagged proteins and callose at the site of fungal attack and at 72 h post-inoculation to score the host cell entry success of *E. cruciferarum*. After infiltration of *Agrobacterium tumefaciens* (Luciferase complementation imaging below for details), *N. benthamiana* plants were transferred to a growth chamber with a photoperiod of 16/8-h d^{-1} light/darkness with a photosynthetic photon flux density of 105 to 120 μmol m^{-2} s^{-1}, an average day/night temperature of 23/20 °C and a relative humidity of 80% to 90%. Post-infiltration incubation was carried out for 3 d. For the analysis of callose, autofluorescence, heavy metal, and ROS phenotypes, the plants were cultivated on Jiffy pellets (Jiffy Products International BV, Zwijndrecht, The Netherlands) at 23/20 °C average day/night temperature with a photoperiod of 16/8-h d^{-1} light/darkness.

Generation of an additional *mlo6* mutant by CRISPR-Cas9-based gene editing

To generate *mlo6-6*, the *mlo6* CRISPR mutant, an expression vector harboring a 2-target gene-specific gRNA was constructed based on a previously published system for multiplex gene editing (Xing et al. 2014). Primers for the *MLO6* gene-specific gRNAs were designed using the CRISPR-P web tool (Lei et al. 2014), and were then used to amplify the target fragments from pCBC-DT1DT2 (https://www.addgene.org/50590/), which were then cloned into vector pHSE401 (https://www.addgene.org/62201/) by Golden Gate cloning (Engler et al. 2008). The final vector expressing the gRNAs was transferred into *Agrobacterium tumefaciens* (strain GV3101) (Koncz and Shell 1986) and *A. thaliana* Col-0 plants were transformed via the floral dip method (Clough and Bent 1998). Transgenic plants were selected based on hygromycin resistance, and the presence of the homozygous deletion was verified by Sanger DNA sequencing. The newly generated *mlo6-6* mutant carries a CRISPR-Cas9-induced 1-bp deletion in a run of 3 consecutive T nucleotides at positions 786 to 788 (numbering is according to the *MLO6* coding sequence; beginning of exon 7). This causes a frameshift leading to a premature stop codon in the *MLO6* coding sequence 19 amino acids downstream of the mutational event (Supplementary Fig. S2, A and B). Oligonucleotides used for the generation of the *mlo6-6* mutant and sequencing are listed in Supplementary Table S2.

Histochemical staining of leaf-attached trichomes for callose and autofluorescence assays

The staining of callose in *A. thaliana* trichomes was carried out as previously described (Kulich et al. 2018). Briefly, leaves were washed for 3 to 4 h in acetic acid:ethanol (1:3) solution and incubated overnight in aniline blue solution (0.01% (m/v) aniline blue in 150-mM potassium dihydrogen phosphate buffer, pH 9.5). For the observation of autofluorescence (as described in the Microscopy section below), the third or fourth visible leaf was used. The leaf was squeezed on the microscope slide and the trichomes were brushed using a needle to stimulate the accumulation of autofluorescent phenolic compounds. Trichomes were then observed under UV illumination after 5 to 10 min without a cover glass using a Nikon Eclipse 90i microscope with a PlanApo 4×/0.2 objective equipped with a Nikon DsFi 2 camera.

Histochemical staining of leaf-attached trichomes for ROS

The detection of hydrogen peroxide as a key representative of ROS was conducted as previously reported (Daudi and O'Brien 2012) using the third or fourth leaf of 3-wk-old plants. The staining was performed 1 h after cutting to stabilize the ROS level in the whole leaf. Leaves were vacuum-infiltrated for 5 min with the DAB solution (1 mg mL^{-1} in 10 mM Na_2HPO_4, 0.05% (v/v) Tween 20) and then incubated on a shaker for 5 h. Following the incubation, the leaves were transferred to 50-mL test tubes containing a bleaching solution (3:1:1 mixture of ethanol, acetic acid, and glycerol) and boiled for 15 to 20 min (until leaves were completely bleached). Following bleaching, leaves were placed in 6-well plates and observed the following day.

Histochemical staining of leaf-attached trichomes for heavy metals

Three-week-old *A. thaliana* plants were watered with a 1-mM zinc chloride solution for 4 consecutive days in 1 wk and stained with dithizone as described previously (Seregin and Ivanov 1997). The staining solution was composed of 30 mg of dithizone dissolved in 20 mL of distilled water, 60 mL of acetone, and 8 drops of acetic acid. The leaves were stained for 1 h and observed the same day. Before observation, each leaf was rinsed in distilled water.

Plasmolysis of leaf-attached trichomes

For plasmolysis, 28-d-old rosette leaves were used and incubated for 1.5 h in a 20% sucrose solution, and then observed by a Zeiss LSM880 NLO with a C-Apochromat 40/1.2 W correction FCS M27 objective. Excitation (in parentheses) and emission wavelengths were as follows: GFP (488 nm, argon laser) 508 to 540 nm and mCherry (561 nm, Diode-Pumped Solid-State 561 laser) 597 to 641 nm.

Trichome isolation

Trichome release and enrichment were carried out according to the STIRRER method introduced previously (Huebbers et al. 2022). Briefly, freshly harvested *A. thaliana* seedlings were transferred to a 500-mL beaker containing 250 mL of phosphate-buffered saline solution (PBS; 10-mM disodium hydrogen phosphate, 2.7-mM potassium chloride, 2.0-mM potassium dihydrogen phosphate, 0.5-mM magnesium chloride, 137-mM sodium chloride, pH 7.5) supplemented with 50-mM ethylenediaminetetraacetic acid (EDTA). The trichome buffer suspension was stirred at 300 rpm for 30 min. Subsequently, 4

layers of screen door mesh (nominal pore size of 1.2 × 1.4 mm) were used to separate the processed seedlings from the buffer solution containing the released trichomes. The trichomes were captured in a 300-mL beaker and poured through a cell strainer (VWR, Radnor, Pennsylvania, USA) with a nominal pore size of 100 μm. These strained trichomes were collected by a small spatula and transferred to 2-mL reaction tubes. After the first round of agitation and filtration, the process was repeated 2 times for 15 min each. Enriched trichomes were either stored at 4 °C in 1-mL phosphate-buffered saline buffer or frozen in liquid nitrogen and lyophilized for monosaccharide and cellulose quantification or FTIR spectroscopy.

Histochemical staining of isolated trichomes

Histochemical staining of *A. thaliana* trichomes was carried out using 20 μL of the appropriate trichome suspension sample, which was mixed with an equal volume of the desired staining solution. Incubation took place in the dark as follows. For calcofluor white, trichomes were incubated for 60 min and samples were observed by UV illumination. For ruthenium red and toluidine blue O, samples were incubated for 120 min and imaged via bright-field illumination. Calcofluor white, ruthenium red, and toluidine blue O solutions were prepared as described previously (Pradhan Mitra and Loqué 2014).

Quantification of neutral sugars and cellulose

The mass of neutral monosaccharides and cellulose in isolated and lyophilized trichomes was determined as described (Yeats et al. 2016). In brief, alcohol-insoluble material was prepared from the dried trichomes and split into 2 samples. One sample was treated with a weak acid (4% sulfuric acid) to release matrix polysaccharide-derived sugars, while the other sample was treated with a strong acid (72% sulfuric acid) to swell cellulose. Afterwards, the solution was adjusted with distilled water to the concentration of the weak acid (4% sulfuric acid) to yield monosaccharides derived from cellulose and the matrix polymers. Subtraction of the 2 values allows for the quantification of crystalline cellulose. Monosaccharides were quantified using a Professional IC Vario high-performance anion-exchange chromatography system (Methrom, Herisau, Switzerland) equipped with a CarboPac PA20 column (Thermo Fisher Scientific, Waltham, Massachusetts, USA) and an amperometric detector (Methrom). The elution gradient of the monosaccharides is specified in Yeats et al. (2016).

Quantification of uronic acids

Isolated and lyophilized trichomes were acid hydrolyzed with 2-N-trifluoroacetic acid at 121 °C and dried under nitrogen flow at 30 °C. Then, the samples were resuspended in miliQ water and assessed by the *m*-hydroxybiphenyl method (Blumenkrantz and Asboe-Hansen 1973) using D-(+)-galacturonic acid (Merck, Darmstadt, Germany) as a standard.

FTIR spectroscopy

FTIR spectra were obtained from isolated and lyophilized trichomes using a JASCO4700 FTIR spectrometer (JASCO, Pfungstadt, Germany) equipped with an attenuated total reflection module (ATR) at a resolution of 1 cm^{-1}. The region between 800 and 1800 cm^{-1} was selected from the average spectra ($n = 10$) to analyze differences in cell wall components (Alonso-Simón et al. 2011). Subsequently, all spectra were normalized and baseline-corrected by using Spectra Manager (JASCO).

Generation of plant expression constructs and transgenic lines

MLO2 and *MLO6* cDNAs and *MLO12* genomic sequences were amplified by PCR using suitable primers and integrated via BP recombination into Gateway-compatible pDONR221 entry vectors (Thermo Fisher Scientific). These *MLO* inserts and the *EXO70H4* genomic sequence were co-shuttled via multisite Gateway recombination into plant expression vectors pK7m34GW (Karimi et al. 2005; *MLO2*) or pH7m34GW (Karimi et al. 2005; *MLO6* and MLO12). Similarly, an *MLO6-GFP* plant expression construct under the control of the *MLO6* promoter was established by multisite Gateway recombination. The resulting binary expression vectors were transferred into *Agrobacterium tumefaciens* strain GV3101 (pMP90RK) (Koncz and Shell 1986), and transgenic *A. thaliana* lines were generated via the floral dip method (Clough and Bent 1998). The selection of transgenic lines was performed on suitable selection media. Likewise, an *MLO2-YFP* plant expression construct driven by *ProCaMV35S* was generated by Gateway recombination. To this end, complementary primers were used for the amplification of *MLO2* cDNA. The *attB* site-containing amplicon was shuttled into pDONR201 (Thermo Fisher Scientific) by Gateway BP recombination. The resulting entry vector was used for LR recombination with pAMPAT-*ProCaMV35S:GWY-mYFP*, a modified version of pAMPAT-*ProCaMV35S:GWY-LUC* (https://www.addgene.org/80678/). Oligonucleotides used for the generation of constructs and sequencing are listed in Supplementary Table S2. The final binary expression vector was transferred into *A. tumefaciens* strain GV3101 (pMP90RK) (Koncz and Shell 1986), and transgenic *A. thaliana* lines were generated by the floral dip method as described above. By analogy, for the expression of GFP-EXO70H4 under the control of the *UBIQUITIN10* promoter, the genomic fragment of *EXO70H4* was subcloned into pDONOR 221 (Thermo Fisher Scientific) using Gateway BP recombination and then transferred into vector pUBN-GFP (Grefen et al. 2010; Kulich et al. 2018) to generate *ProUBQ10:GFP-EXO70H4*, which was transformed into Col-0 WT plants by the floral dip method (see above).

Microscopy

The observation of callose and autofluorescence for leaf-attached trichomes was done using a Nikon Eclipse 90i microscope equipped with either a PlanApo 4×/0.2 objective

(for the quantification of callose and the acquisition of autofluorescence) or a PlanApo 10×/0.45 objective (for imaging single trichomes). Micrographs were captured with a Nikon DsFi 2 camera. For the observation of ROS, an Olympus IX71 microscope equipped with a LUCPlanFLN 40×/0.6 objective was used. For imaging of heavy metal depositions, a Nikon Eclipse 90i microscope equipped with a PlanApo 20×/0.75 objective was used. Trichome cell wall thickness was observed with an Olympus BX51 microscope equipped with a UPlanSApo 60×/1.20 water immersion objective. Brightfield micrographs were captured and cell wall thickness was assessed at the region of the OR (Supplementary Fig. S12). Micrographs of histochemically stained isolated trichomes were captured using a BZ-9000 transmitted light and epifluorescence microscope (Keyence, Osaka, Japan).

For confocal microscopy of trichomes, a Zeiss LSM880 NLO with a C-Apochromat 40/1.2 W correction FCS M27 objective was used. Excitation (in parentheses) and emission wavelengths were as follows: GFP (488 nm) 508 to 540 nm, chlorophyll (402 nm) 650 to 721 nm, cell wall autofluorescence (405 nm) 426 to 502 nm, mCherry (561 nm) 597 to 641 nm, as described before (Kulich et al. 2018). The focal accumulation of fluorophore-tagged proteins and callose at the penetration site of *E. cruciferarum* was observed with a Leica SP8 confocal laser scanning microscope equipped with a 63 × water correction objective using the following wavelengths for excitation (in parentheses) and emission: GFP (496, argon laser) 505 to 514 nm, YFP (514 nm, argon laser) 522 to 536 nm, mCherry (561 nm, Diode-Pumped Solid-State 561 laser) 590 to 620 nm, and aniline blue (405 nm, Diode 405) 488 to 496 nm.

Image analysis

All micrographs of leaf-attached trichomes were processed using the Fiji platform as described below. To calculate the number of stable PM-associated GFP-PMR4- and MLO6-GFP-marked dots (compartments) in *A. thaliana* trichomes, we imaged the trichomes in a time-series experiment and subsequently performed the minimal projections command in the Fiji software (Schindelin et al. 2012; Kulich et al. 2018). We then calculated the number of visible dots using the dot and ROI Manager tools. Image optimization for micrographs of histochemically stained isolated trichomes was carried out identically for all micrographs of the same staining type using Adobe Photoshop 2022.

Colocalization analysis of fluorophore-tagged proteins in mature rosette leaf trichomes was performed using Fiji JACoP (Just Another Colocalization Plugin; Bolte and Cordelières 2006). For each transgenic line, we examined 5 images from 4 different experimental replicates, consisting of 2 frames taken in immediate succession. Each frame combination was analyzed to obtain Pearson's correlation coefficient, and based on this, the RBNCC (Replicate-Based Noise Corrected Correlation) coefficient was calculated as described before (Daly et al. 2012) to obtain a noise-corrected indicator of correlation.

Luciferase complementation imaging

N. benthamiana plants were used for transient gene expression with *A. tumefaciens* harboring the appropriate constructs and the p19 silencing suppressor plasmid, as described before (Campe et al. 2016) with minor modifications. *A. tumefaciens* strain GV3101 (pMP90RK) (Koncz and Schell 1986) was transformed with plasmids harboring different *EXO70* and *MLO* coding sequences that were transferred from pDONR207 entry clones into pAMPAT-CLuc-GWY and pAMPAT-GWY-NLuc vectors (Gruner et al. 2021) via Gateway recombination. Oligonucleotides used for the generation of constructs and sequencing are listed in Supplementary Table S2. For leaf infiltration of agrobacteria, bacterial cultures were grown overnight and resuspended in an infiltration medium (10-mM MES, pH 5.6, 10-mM $MgCl_2$, 150-μM acetosyringone), adjusted to an OD_{600} of 0.5, and incubated at room temperature for 2 h. For co-infiltration, equal volumes of each *A. tumefaciens* strain were mixed and infiltrated into the abaxial side of fully expanded leaves of 4 to 6-wk-old *N. benthamiana* plants with a syringe lacking a cannula. Luciferase complementation was assessed at 2 d after infiltration by spraying the transformed leaves of *N. benthamiana* with 1-mM D-luciferin (PerkinElmer, Rodgau, Germany) dissolved in water supplemented with 0.01% (v/v) Tween-20. Leaves were kept in the dark for 10 min before luminescence was detected with a ChemiDoc XRS+ imaging system (BioRad, Feldkirchen, Germany). Luminescence intensities per square millimeter were evaluated using the Image Lab software (BioRad, Feldkirchen, Germany).

FRET-FLIM analysis

For FRET-FLIM experiments, constructs were transiently expressed in leaves of *N. benthamiana* plants, similarly as described above for the luciferase complementation assays but with an OD_{600} of 0.4 for the agrobacteria. We used MLO6-GFP, mCherry-EXO70H4, and a GFP-mCherry positive control, all expressed under the control of the constitutive *ProCaMV35S*. The analysis was performed at 2 d after agroinfiltration with a Zeiss LSM880 NLO confocal microscope as described above, equipped with a hybrid single photon detector (HPM-100-40; Becker et al. 2011) connected to the Becker & Hickl SPC-150 module (Becker & Hickl GmbH, Berlin, Germany), and using a single band emission filter (AHF 525/50). The images were analyzed using SPCImage software (Becker & Hickl), and donor fluorescence lifetimes were calculated using pixels in the various regions of interest based on color-coded lifetime images (see Supplementary Fig. S7C for examples).

Yeast two-hybrid assays

For yeast two-hybrid assays, *S. cerevisiae* cells were transformed with plasmids expressing EXO70D3, EXO70H4, and either the IC2 or CT fragment of MLO6, respectively. The MLO6 IC2 fragment ($MLO6^{IC2}$) consists of MLO6 amino acid residues 183 to 284, and the MLO6 CT fragment ($MLO6^{CT}$) consists of MLO6 amino acid residues 433 to 583. For cloning of these constructs

EXO70D3, *EXO70H4*, *AtMLO6*^{IC2}, and *AtMLO6*^{CT} coding sequences were mobilized from pDONR207 entry clones via Gateway recombination into yeast two-hybrid vectors pGADT7 and pGBKT7 (Clonetech Laboratories Inc., Mountain View, California, USA). Oligonucleotides used for the generation of constructs and sequencing are listed in Supplementary Table S2. The recombinant plasmids were transformed by the LiAc/PEG method (Gietz and Woods 2002) into *S. cerevisiae* strain AH109. Yeast transformants expressing the recombinant proteins (see below) were spotted on a medium lacking leucine and tryptophan for growth control, and on a medium lacking leucine, tryptophan, and histidine to detect putative interactions. For these tests, yeast cells were grown overnight in liquid synthetic complete medium (James et al. 1996) lacking leucine and tryptophan at 28 °C and 250 rpm. The cells were harvested the following day by 1 min of centrifugation at 3,000 × *g* and washed with sterile water before adjusting the OD_{600} of the solutions to 1. Ten-fold dilution series were established over 4 orders of magnitude and 3 or 4 μL per dilution and construct combination were spotted onto the aforementioned media.

Total phenolic protein extraction

Frozen *N. benthamiana* leaf tissue samples were homogenized for total phenolic protein extraction. The phenolic total protein extractions were performed as described previously (Thomas et al. 2015) with minor changes. The homogenized tissue samples were washed twice with ice-cold acetone and the samples were pelleted between washing steps at 16,000 × *g* for 5 min at 4 °C, before being resuspended in 10% (m/v) trichloroacetic acid (TCA) in acetone. After resuspension, the samples were transferred into an ultrasonic ice water bath for 10 min. Following sonification, the samples were pelleted again for 5 min at 16,000 × *g* (4 °C). The pellets were washed once with 10% (m/v) TCA in acetone, once with 10% (m/v) TCA, and then with 80% (v/v) acetone, samples were resuspended and pelleted (16,000 × *g*, 4 °C, 5 min) between washing steps. The pellets were air-dried briefly and resuspended in freshly prepared dense sodium dodecyl sulfate (SDS) buffer (100-mM Tris-HCl, pH 8.0; 30% (m/v) saccharose; 2% (m/v) SDS; 50-mM dithiothreitol) at room temperature, before adding phenol/Tris-HCl (pH 8.0; AppliChem, Darmstadt, Germany) and thoroughly mixing the samples until they became whitish. The upper phenolic phase was separated by centrifugation (16,000 × *g*, 20 min, room temperature) and proteins were recovered by precipitation for 60 min at −20 °C with 5 volumes of 100-mM (v/v) ammonium acetate in methanol. After a final centrifugation step (16,000 × *g*, 5 min, 4 °C), the protein pellets were washed once with 100-mM (v/v) ammonium acetate in methanol and once with 80% (v/v) acetone.

SDS-PAGE and immunoblot analysis

Separation of proteins was carried out via SDS-polyacrylamide gel electrophoresis (SDS-PAGE). Protein samples were resuspended in NuPAGE LDS Sample buffer (Thermo Fisher Scientific) and denatured by boiling at 95 °C for 5 min before gel loading. Subsequently, 5 μg of total protein was subjected to SDS-PAGE, transferred to a nitrocellulose membrane (Carl Roth, Karlsruhe, Germany), and used for immunoblot detection according to the manufacturer's instructions. For luciferase fusion proteins, an α-luciferase antibody (Merck, Darmstadt, Germany) was used in a 1:1,000 dilution in 5% (m/v) milk in Tris-buffered saline with Tween-20 (TBST; 0.1% (v/v) Tween-20, 0.14-M sodium chloride, 0.02-M Tris, pH 7.6). For Gal4 fusion proteins, α-Gal4BD and α-Gal4AD antibodies (both Santa Cruz Biotechnology, Dallas, Texas, USA) were used in a 1:1,000 dilution in 5% (m/v) milk in TBST. A goat or mouse α-rabbit antibody coupled to horseradish peroxidase (Santa Cruz Biotechnology Inc., Dallas, USA) in a 1:2,000 dilution in 5% (m/v) milk in TBST was used as the secondary antibody to detect luciferase and Gal4 fusion proteins, respectively (for a compilation of the antibodies used in this study see Supplementary Table S3). Chemiluminescence detection of antigen-antibody complexes was carried out with SuperSignal West Femto Western substrate (Thermo Fisher Scientific). As a loading control, the nitrocellulose membrane was stained with a Ponceau S (AppliChem, Darmstadt, Germany) solution (5% acetic acid, 0.5% (m/v) Ponceau S).

Assessment of entry of *E. cruciferarum* into host cells

Inoculum of *E. cruciferarum* for pathogenicity assays was propagated on super-susceptible *A. thaliana eds1-1* mutant plants. Healthy test plants were inoculated by leaf-to-leaf contact, i.e. touching and gently rubbing an infected rosette leaf with profusely sporulating fungal colonies of an inoculum plant against a noninfected, healthy leaf of a test plant. Typically, all mature rosette leaves of test plants were inoculated by this procedure. Two rosette leaves per *A. thaliana* plant were harvested at 72 h post-inoculation and rosette leaves were bleached in denatured ethanol (80.0% (v/v)) at 37 °C. After 72 h of bleaching, leaves were stained with Coomassie Brilliant Blue solution (10.0% (v/v) acetic acid, 0.5% (m/v) Coomassie Brilliant Blue, 45.0% (v/v) methanol), rinsed in distilled water and subjected to brightfield microscopy using an Axiophot microscope (Carl Zeiss, Jena, Germany). Samples were randomized and the host cell entry rate of *E. cruciferarum* on the different genotypes was assessed blindly, i.e. the person scoring did not know the identity of the respective genotypes. To this end, spores that developed secondary hyphae were scored as successful host cell entry, whereas spores that developed an appressorium only were scored as failed host cell entry. The host cell entry rate was calculated as the number of spores exhibiting successful host cell entry divided by the total spore count. Per replicate, at least 100 spores were assessed on 2 rosette leaves derived from a single plant. Overall, 8 independent experiments with 3 replicates each were carried out per genotype.

To investigate the accumulation of callose at the site of fungal attack, rosette leaves of *A. thaliana* were sampled at 24 h post-inoculation and bleached in denatured ethanol as described above. Leaf discs (6-mm diameter) were

prepared and submerged in aniline blue solution (0.01% (m/v) aniline blue in 150-mM dipotassium hydrogen phosphate buffer, pH 8.5) for 1 h, rinsed with distilled water, and subjected to microscopy as described previously for the Leica SP8 confocal laser scanning microscope equipped with a 63× water correction objective.

Computation and statistical procedures

R v.4.1.3 (R foundation, www.r-project.org/) was used for plotting, statistical analyses, and filtering of data during this study. Plotting was carried out using the ggplot2 library whereas data processing was facilitated by the dplyr library, both included in the Tidyverse package (Wickham et al. 2019). Box plots were assembled in the style of Tukey: The boundaries of the whiskers are defined by the lowest or highest value, respectively, within a 1.5 times interquartile range. The box marks the range between the first and third quartiles. Horizontal bars represent the median. Note that in the text, the arithmetic mean was used to compare different samples. Analysis of FTIR spectra by PCA was accomplished using factoextra (Kassambara and Mundt 2020) and FactoMineR (Lê et al. 2008). Absolute (tissue-specific) or relative (biotic stress) transcript data were retrieved from http://bar.utoronto.ca/efp/cgi-bin/efpWeb.cgi on April 19, 2021. Correlation analysis of these transcript data was facilitated by the corrplot package (Wei and Simko 2021). We assessed the distribution of our data by quantile–quantile plots and by the Shapiro–Wilk test ($\alpha = 0.05$; Shapiro and Wilk 1965) and checked for homoscedasticity (equality of variances) by Levene's test ($\alpha = 0.05$; Gastwirth et al. 2009). Normally distributed data with similar variances were subjected to Student's *t*-test (Student 1908), whereas statistical differences between non-normally distributed samples were reviewed by the Wilcoxon–Mann–Whitney test (Mann and Whitney 1947). Pearson's chi-square test (Pearson 1900) was used to assess the statistical differences between nominal data. In the case of multiple comparison hypothesis testing, FDR was used to correct for the increased probability of type I errors (Benjamini and Hochberg 1995). Results of detailed statistical analyses are presented in Supplementary Data Set 1.

Accession numbers

EXO70B2 (At1g07000), EXO70D3 (At3g14090), EXO70H1 (At3g55150), EXO70H2 (At2g39380), EXO70H4 (At3g09520), EXO70H7 (At5g59730), GSL5/PMR4 (At4g03550), MLO2 (At1g11310), MLO6 (At1g61560), and MLO12 (At2g39200).

Acknowledgments

We thank Franz Leissing for suggestions and critical discussions regarding the project, Marie Laufens for scoring powdery mildew infection phenotypes of various *A. thaliana* genotypes, and Lorena Meusel for providing the positive control used for FRET-FLIM experiments.

Author contributions

J.W.H. carried out histochemical staining of isolated trichomes, prepared trichome samples for monosaccharide and cellulose quantification and FTIR spectroscopy, analyzed cell wall and transcript data, performed luciferase complementation imaging and yeast two-hybrid experiments, carried out immunoblot analysis, assessed the powdery mildew infection phenotypes of *A. thaliana* WT and mutant plants, designed the figures, and performed statistical analysis. G.A.C. generated constructs of fluorophore-labeled proteins, established transgenic lines, performed histochemical staining of leaf-attached trichomes, generated the *mlo6* CRISPR line, performed microscopy, yeast two-hybrid experiments, and FRET-FLIM experiments, and conducted image analysis and statistical analysis. V.Ž. participated in the planning of the experiments, cloned constructs for the visualization of fluorophore-labeled proteins, generated and characterized transgenic lines, performed microscopy, characterized phenotypic deviations in mutant trichomes, and assisted in data interpretation. P.S. generated transgenic lines, performed microscopy, and conducted image analysis. S.C.J.L. performed luciferase complementation imaging assays and yeast two-hybrid experiments and conducted the related immunoblot analyses. H.K. discovered the phenotypic overlap between *mlo2 mlo6 mlo12* triple mutants and the *exo70H4* mutant and, together with A.R., generated the transgenic MLO2-YFP line. I.K. contributed to study conception together with H.K. A.R. generated constructs, including the transgenic MLO2-YFP line (together with H.K.), and selected higher-order mutant lines. K.B. contributed to trichome sampling for biochemical carbohydrate measurements and established histochemical staining experiments with isolated trichomes. A.M.-R. and H.M. performed FTIR experiments and analyzed uronic acid content. M.P. performed the biochemical analysis of neutral carbohydrates and cellulose. R.P. and V.Ž. conceived the study. G.A.C., P.S., J.W.H., and R.P. drafted and edited the manuscript.

Supplementary data

The following materials are available in the online version of this article.

Supplementary Figure S1. Quantification of trichome phenotypes in *exo70H4-1* and *mlo* mutants.

Supplementary Figure S2. Rosette leaf trichomes of the CRISPR/Cas9-derived *mlo6-6* mutant show phenotypes reminiscent of *mlo6-2* mutant trichomes.

Supplementary Figure S3. *A. thaliana exo70H4* and *mlo2 mlo6 mlo12* triple mutants have altered trichome cell wall characteristics.

Supplementary Figure S4. Trichome age does not affect the colocalization of *A. thaliana* clade V MLO proteins and EXO70H4.

Supplementary Figure S5. Colocalization details of fluorophore-tagged EXO70H4 and MLO proteins in trichomes of transgenic lines.

Supplementary Figure S6. Analysis of the interaction of MLO6 with various EXO70 proteins by LCI.

Supplementary Figure S7. Representative luminescence signals and validation of protein production in leaves of *N. benthamiana* after luciferase complementation imaging.

Supplementary Figure S8. Yeast two-hybrid assays suggest an interaction of EXO70H4, but not EXO70D3, with the carboxy terminus of MLO6.

Supplementary Figure S9. Additive and synergistic reduction of *E. cruciferarum* entry rates in *exo70H4-1 mlo2-5* and *exo70H4-1 mlo6* double mutants.

Supplementary Figure S10. Fluorophore-tagged EXO70H4 accumulates weakly at attempted pathogen entry sites.

Supplementary Figure S11. *exo70H4* and *mlo* mutants are not evidently impaired regarding the accumulation of callose at attempted powdery mildew entry sites.

Supplementary Figure S12. Measurement of trichome cell wall thickness.

Supplementary Table S1. Wavenumber regions and their assignment to cell wall compounds according to the literature.

Supplementary Table S2. Sequences of oligonucleotides used in this study.

Supplementary Table S3. Antibodies used in this study.

Supplementary Data Set 1. Statistical analysis results.

Supplementary Movie S1. Mobility of fluorescent MLO6-GFP-containing compartments in Col-0 WT.

Supplementary Movie S2. Mobility of fluorescent MLO6-GFP-containing compartments in the *exo70H4-1* mutant.

Supplementary Movie Legends.

Funding

This project was funded by a joint DFG-GACR funding scheme. Individual funds were provided by Grant PA 861/20-1 (project number 411779037) of the Deutsche Forschungsgemeinschaft (DFG; German Research Foundation) to R.P. and Czech Science Foundation/GACR international project number GC19-02242J to V.Ž. Additionally, part of the income for V.Ž. was provided by the Ministry of Education, Youth and Sports of CR/MŠMT proj. EXBIO -CZ.02.1.01/0.0/0.0/16_019/0000738. Research in the H.M. lab was financially supported by Grant PID2020-120364GA-I00 of the Spanish Ministry of Science and Innovation. Part of the microscopy was performed in the Vinicna Microscopy Core Facility and was co-financed by the Czech-BioImaging large RI project LM2023050. The confocal microscope used at RWTH Aachen University was purchased via DFG Grant ZUK 32/2013 (A659). Computational resources were supplied by the project e-Infrastruktura CZ (e-INFRA LM2018140) provided within the program Projects of Large Research, Development and Innovations Infrastructures.

Conflict of interest statement. None declared.

Data availability

All relevant data can be found within the manuscript and its supporting materials.

References

Acevedo-Garcia J, Gruner K, Reinstädler A, Kemen A, Kemen E, Cao L, Takken FLW, Reitz MU, Schäfer P, O'Connell RJ, et al. The powdery mildew-resistant Arabidopsis *mlo2 mlo6 mlo12* triple mutant displays altered infection phenotypes with diverse types of phytopathogens. Sci Rep. 2017:**7**(1):9319. https://doi.org/10.1038/s41598-017-07188-7

Albertazzi L, Arosio D, Marchetti L, Ricci F, Beltram F. Quantitative FRET analysis with the EGFP-mCherry fluorescent protein pair. Photochem Photobiol. 2009:**85**(1):287–297. https://doi.org/10.1111/j.1751-1097.2008.00435.x

Alonso-Simón A, García-Angulo P, Mélida H, Encina A, Álvarez JM, Acebes JL. The use of FTIR spectroscopy to monitor modifications in plant cell wall architecture caused by cellulose biosynthesis inhibitors. Plant Signal Behav. 2011:**6**(8):1104–1110. https://doi.org/10.4161/psb.6.8.15793

Assaad FF, Qiu JL, Youngs H, Ehrhardt D, Zimmerli L, Kalde M, Wanner G, Peck SC, Edwards H, Ramonell K, et al. The PEN1 syntaxin defines a novel cellular compartment upon fungal attack and is required for the timely assembly of papillae. Mol Biol Cell. 2004:**15**(11):5118–5129. https://doi.org/10.1091/mbc.e04-02-0140

Barclay JW, Morgan A, Burgoyne RD. Calcium-dependent regulation of exocytosis. Cell Calcium. 2005:**38**(3-4):343–353. https://doi.org/10.1016/j.ceca.2005.06.012

Bastiaens PI, Squire A. Fluorescence lifetime imaging microscopy: spatial resolution of biochemical processes in the cell. Trends Cell Biol. 1999:**9**(2):48–52. https://doi.org/10.1016/S0962-8924(98)01410-X

Becker W, Su B, Holub O, Weisshart K. FLIM and FCS detection in laser-scanning microscopes: increased efficiency by GaAsP hybrid detectors. Microsc Res Tech. 2011:**74**(9):804–811. https://doi.org/10.1002/jemt.20959

Bednarek P, Piślewska-Bednarek M, Svatoš A, Schneider B, Doubský J, Mansurova M, Humphry M, Consonni C, Panstruga R, Sanchez-Vallet A, et al. A glucosinolate metabolism pathway in living plant cells mediates broad-spectrum antifungal defense. Science. 2009:**323**(5910):101–106. https://doi.org/10.1126/science.1163732

Benjamini Y, Hochberg Y. Controlling the false discovery rate—a practical and powerful approach to multiple testing. J R Stat Soc Ser B Methodol. 1995:**57**(1):289–300. https://doi.org/10.1111/j.2517-6161.1995.tb02031.x

Bhat RA, Miklis M, Schmelzer E, Schulze-Lefert P, Panstruga R. Recruitment and interaction dynamics of plant penetration resistance components in a plasma membrane microdomain. Proc Natl Acad Sci U S A. 2005:**102**(8):3135–3140. https://doi.org/10.1073/pnas.0500012102

Bidzinski P, Noir S, Shahi S, Reinstädler A, Gratkowska DM, Panstruga R. Physiological characterization and genetic modifiers of aberrant root thigmomorphogenesis in mutants of *Arabidopsis thaliana MILDEW LOCUS O* genes. Plant Cell Environ. 2014:**37**(12):2738–2753. https://doi.org/10.1111/pce.12353

Blumenkrantz N, Asboe-Hansen G. New method for quantitative determination of uronic acids. Anal Biochem. 1973:**54**(2):484–489. https://doi.org/10.1016/0003-2697(73)90377-1

Bolte S, Cordelières FP. A guided tour into subcellular colocalization analysis in light microscopy. J Microsc. 2006:**224**(3):213–232. https://doi.org/10.1111/j.1365-2818.2006.01706.x

Büschges R, Hollricher K, Panstruga R, Simons G, Wolter M, Frijters A, van Daelen R, van der Lee T, Diergaarde P, Groenendijk J, et al. The barley *Mlo* gene: a novel control element of plant pathogen resistance. Cell. 1997:**88**(5):695–705. https://doi.org/10.1016/S0092-8674(00)81912-1

Campe R, Langenbach C, Leissing F, Popescu GV, Popescu SC, Goellner K, Beckers GJ, Conrath U. ABC transporter PEN3/PDR8/ABCG36 interacts with calmodulin that, like PEN3, is required for Arabidopsis nonhost resistance. New Phytol. 2016:**209**(1):294–306. https://doi.org/10.1111/nph.13582

Chen H, Zou Y, Shang Y, Lin H, Wang Y, Cai R, Tang X, Zhou J-M. Firefly Luciferase Complementation Imaging assay for protein-protein interactions in plants. Plant Physiol. 2008:**146**(2):323–324. https://doi.org/10.1104/pp.107.111740

Chen Z, Noir S, Kwaaitaal M, Hartmann HA, Wu MJ, Mudgil Y, Sukumar P, Muday G, Panstruga R, Jones AM. Two seven-transmembrane domain MILDEW RESISTANCE LOCUS O proteins cofunction in *Arabidopsis* root thigmomorphogenesis. Plant Cell. 2009:**21**(7):1972–1991. https://doi.org/10.1105/tpc.108.062653

Chiniquy D, Underwood W, Corwin J, Ryan A, Szemenyei H, Lim CC, Stonebloom SH, Birdseye DS, Vogel J, Kliebenstein D, et al. PMR5, an acetylation protein at the intersection of pectin biosynthesis and defense against fungal pathogens. Plant J. 2019:**100**(5):1022–1035. https://doi.org/10.1111/tpj.14497

Clough SJ, Bent AF. Floral dip: a simplified method for *Agrobacterium*-mediated transformation of *Arabidopsis thaliana*. Plant J. 1998:**16**(6): 735–743. https://doi.org/10.1046/j.1365-313x.1998.00343.x

Collins NC, Thordal-Christensen H, Lipka V, Bau S, Kombrink E, Qiu JL, Hückelhoven R, Stein M, Freialdenhoven A, Somerville SC, et al. SNARE-protein-mediated disease resistance at the plant cell wall. Nature. 2003:**425**(6961):973–977. https://doi.org/10.1038/nature02076

Consonni C, Bednarek P, Humphry M, Francocci F, Ferrari S, Harzen A, Ver Loren van Themaat E, Panstruga R. Tryptophan-derived metabolites are required for antifungal defense in the Arabidopsis *mlo2* mutant. Plant Physiol. 2010:**152**(3):1544–1561. https://doi.org/10.1104/pp.109.147660

Consonni C, Humphry ME, Hartmann HA, Livaja M, Durner J, Westphal L, Vogel J, Lipka V, Kemmerling B, Schulze-Lefert P, et al. Conserved requirement for a plant host cell protein in powdery mildew pathogenesis. Nat Genet. 2006:**38**(6):716–720. https://doi.org/10.1038/ng1806

Cui F, Wu H, Safronov O, Zhang P, Kumar R, Kollist H, Salojärvi J, Panstruga R, Overmyer K. Arabidopsis MLO2 is a negative regulator of sensitivity to extracellular reactive oxygen species. Plant Cell Environ. 2018:**41**(4):782–796. https://doi.org/10.1111/pce.13144

Cvrčková F, Grunt M, Bezvoda R, Hála M, Kulich I, Rawat A, Žárský V. Evolution of the land plant exocyst complexes. Front Plant Sci. 2012:**3**:159. https://doi.org/10.3389/fpls.2012.00159

Daly CJ, Parmryd I, McGrath JC. Visualization and analysis of vascular receptors using confocal laser scanning microscopy and fluorescent ligands. Methods Mol Biol. 2012:**897**:95–107. https://doi.org/10.1007/978-1-61779-909-9_5

Daudi A, O'Brien JA. Detection of hydrogen peroxide by DAB staining in *Arabidopsis* leaves. Bio Protoc. 2012:**2**(18):e263e263. https://doi.org/10.21769/BioProtoc.263

Devoto A, Hartmann HA, Piffanelli P, Elliott C, Simmons C, Taramino G, Goh CS, Cohen FE, Emerson BC, Schulze-Lefert P, et al. Molecular phylogeny and evolution of the plant-specific seven-transmembrane MLO family. J Mol Evol. 2003:**56**(1):77–88. https://doi.org/10.1007/s00239-002-2382-5

Devoto A, Piffanelli P, Nilsson I, Wallin E, Panstruga R, von Heijne G, Schulze-Lefert P. Topology, subcellular localization, and sequence diversity of the Mlo family in plants. J Biol Chem. 1999:**274**(49): 34993–35004. https://doi.org/10.1074/jbc.274.49.34993

Elias M, Drdova E, Ziak D, Bavlnka B, Hala M, Cvrckova F, Soukupova H, Žárský V. The exocyst complex in plants. Cell Biol Int. 2003:**27**(3): 199–201. https://doi.org/10.1016/S1065-6995(02)00349-9

Elliott C, Müller J, Miklis M, Bhat RA, Schulze-Lefert P, Panstruga R. Conserved extracellular cysteine residues and cytoplasmic loop–loop interplay are required for functionality of the heptahelical MLO protein. Biochem J. 2005:**385**(1):243–254. https://doi.org/10.1042/BJ20040993

Engler C, Kandzia R, Marillonnet S. A one pot, one step, precision cloning method with high throughput capability. PLoS One. 2008:**3**(11):e3647. https://doi.org/10.1371/journal.pone.0003647

Eschrich W, Currier HB. Identification of cauose by its diachrome and fluorochrome reactions. Stain Technol. 1964:**39**(5):303–307. https://doi.org/10.3109/10520296409061248

Falk A, Feys BJ, Frost LN, Jones JD, Daniels MJ, Parker JE. *EDS1*, an essential component of R gene-mediated disease resistance in *Arabidopsis* has homology to eukaryotic lipases. Proc Natl Acad Sci U S A. 1999:**96**(6):3292–3297. https://doi.org/10.1073/pnas.96.6.3292

Fendrych M, Synek L, Pečenková T, Drdová EJ, Sekeres J, de Rycke R, Nowack MK, Zársky V. Visualization of the exocyst complex dynamics at the plasma membrane of *Arabidopsis thaliana*. Mol Biol Cell. 2013:**24**(4):510–520. https://doi.org/10.1091/mbc.e12-06-0492

Folkers U, Berger J, Hülskamp M. Cell morphogenesis of trichomes in *Arabidopsis*: differential control of primary and secondary branching by branch initiation regulators and cell growth. Development. 1997:**124**(19):3779–3786. https://doi.org/10.1242/dev.124.19.3779

Fujisaki K, Abe Y, Ito A, Saitoh H, Yoshida K, Kanzaki H, Kanzaki E, Utsushi H, Yamashita T, Kamoun S, et al. Rice Exo70 interacts with a fungal effector, AVR-Pii, and is required for AVR-Pii-triggered immunity. Plant J. 2015:**83**(5):875–887. https://doi.org/10.1111/tpj.12934

Gao Q, Wang C, Xi Y, Shao Q, Li L, Luan S. A receptor–channel trio conducts Ca^{2+} signalling for pollen tube reception. Nature. 2022:**607**(7919): 534–539. https://doi.org/10.1038/s41586-022-04923-7

Gastwirth JL, Gel YR, Miao W. The impact of Levene's test of equality of variances on statistical theory and practice. Statist Sci. 2009:**24**(3): 343–360. https://doi.org/10.1214/09-STS301

Gietz RD, Woods RA. Transformation of yeast by lithium acetate/single-stranded carrier DNA/polyethylene glycol method. In: **Fink GR, Guthrie C**, editors. Guide to yeast genetics and molecular and cell biology. Amsterdam: Academic Pr; 2002. p. 87–96.

Gilding EK, Marks MD. Analysis of purified glabra3-shapeshifter trichomes reveals a role for NOECK in regulating early trichome morphogenic events. Plant J. 2010:**64**(2):304–317. https://doi.org/10.1111/j.1365-313X.2010.04329.x

Grefen C, Donald N, Hashimoto K, Kudla J, Schumacher K, Blatt MR. A ubiquitin-10 promoter-based vector set for fluorescent protein tagging facilitates temporal stability and native protein distribution in transient and stable expression studies. Plant J. 2010:**64**(2): 355–365. https://doi.org/10.1111/j.1365-313X.2010.04322.x

Gruner K, Leissing F, Sinitski D, Thieron H, Axstmann C, Baumgarten K, Reinstädler A, Winkler P, Altmann M, Flatley A, et al. Chemokine-like MDL proteins modulate flowering time and innate immunity in plants. J Biol Chem. 2021:**296**:100611. https://doi.org/10.1016/j.jbc.2021.100611

Gruner K, Zeier T, Aretz C, Zeier J. A critical role for Arabidopsis MILDEW RESISTANCE LOCUS O2 in systemic acquired resistance. Plant J. 2018:**94**(6):1064–1082. https://doi.org/10.1111/tpj.13920

Gupta C, Pereira A. Recent advances in gene function prediction using context-specific coexpression networks in plants. F1000Res. 2019:**8**: F1000 Faculty Rev-153. https://doi.org/10.12688/f1000research.17207.1

Heider MR, Munson M. Exorcising the exocyst complex. Traffic. 2012:**13**(7):898–907. https://doi.org/10.1111/j.1600-0854.2012.01353.x

Holden S, Bergum M, Green P, Bettgenhaeuser J, Hernández-Pinzón I, Thind A, Clare S, Russell JM, Hubbard A, Taylor J, et al. A lineage-specific Exo70 is required for receptor kinase–mediated immunity in barley. Sci Adv. 2022:**8**(27):eabn7258. https://doi.org/10.1126/sciadv.abn7258

Huebbers JW, Büttgen K, Leissing F, Mantz M, Pauly M, Huesgen PF, Panstruga R. An advanced method for the release, enrichment and purification of high-quality *Arabidopsis thaliana* rosette leaf trichomes enables profound insights into the trichome proteome. Plant Methods. 2022:**18**(1):12. https://doi.org/10.1186/s13007-021-00836-0

Hülskamp M, Misŕa S, Jürgens G. Genetic dissection of trichome cell development in Arabidopsis. Cell. 1994:**76**(3):555–566. https://doi.org/10.1016/0092-8674(94)90118-X

Humphry M, Bednarek P, Kemmerling B, Koh S, Stein M, Göbel U, Stüber K, Piślewska-Bednarek M, Loraine A, Schulze-Lefert P, et al. A regulon conserved in monocot and dicot plants defines a functional module in antifungal plant immunity. Proc Natl Acad Sci U S A. 2010:**107**(50):21896–21901. https://doi.org/10.1073/pnas.1003619107

Jacobs AK, Lipka V, Burton RA, Panstruga R, Strizhov N, Schulze-Lefert P, Fincher GB. An Arabidopsis callose synthase, GSL5, is required for wound and papillary callose formation. Plant Cell. 2003:**15**(11):2503–2513. https://doi.org/10.1105/tpc.016097

Jakoby MJ, Falkenhan D, Mader MT, Brininstool G, Wischnitzki E, Platz N, Hudson A, Hülskamp M, Larkin J, Schnittger A. Transcriptional profiling of mature Arabidopsis trichomes reveals that NOECK encodes the MIXTA-like transcriptional regulator MYB106. Plant Physiol. 2008:**148**(3):1583–1602. https://doi.org/10.1104/pp.108.126979

James P, Halladay J, Craig EA. Genomic libraries and a host strain designed for highly efficient two-hybrid selection in yeast. Genetics. 1996:**144**(4):1425–1436. https://doi.org/10.1093/genetics/144.4.1425

Jørgensen JH. Discovery, characterization and exploitation of Mlo powdery mildew resistance in barley. Euphytica. 1992:**63**(1–2):141–152. https://doi.org/10.1007/BF00023919

Ju Y, Yuan J, Jones DS, Zhang W, Staiger CJ, Kessler SA. Polarized NORTIA accumulation in response to pollen tube arrival at synergids promotes fertilization. Dev Cell. 2021:**56**(21):2938–2951.e6. https://doi.org/10.1016/j.devcel.2021.09.026

Karimi M, de Meyer B, Hilson P. Modular cloning in plant cells. Trends Plant Sci. 2005:**10**(3):103–105. https://doi.org/10.1016/j.tplants.2005.01.008

Kassambara A, Mundt F. Factoextra: Extract and visualize the results of multivariate data analyses. R Package Version 1.0.7. 2020. https://CRAN.R-project.org/package=factoextra

Kessler SA, Shimosato-Asano H, Keinath NF, Wuest SE, Ingram G, Panstruga R, Grossniklaus U. Conserved molecular components for pollen tube reception and fungal invasion. Science. 2010:**330**(6006):968–971. https://doi.org/10.1126/science.1195211

Kim MC, Panstruga R, Elliott C, Müller J, Devoto A, Yoon HW, Park HC, Cho MJ, Schulze-Lefert P. Calmodulin interacts with MLO protein to regulate defence against mildew in barley. Nature. 2002:**416**(6879):447–450. https://doi.org/10.1038/416447a

Kim S, Kim H, Park K, Cho DJ, Kim MK, Kwon C, Yun HS. Synaptotagmin 5 controls SYP132–VAMP721/722 interaction for Arabidopsis immunity to *Pseudomonas syringae* pv *tomato* DC3000. Mol Cells. 2021:**44**(9):670–679. https://doi.org/10.14348/molcells.2021.0100

Koncz C, Schell J. The promoter of TL-DNA gene 5 controls the tissue-specific expression of chimaeric genes carried by a novel type of *Agrobacterium* binary vector. Mol Gen Genet. 1986:**204**(3):383–396. https://doi.org/10.1007/BF00331014

Kubátová Z, Pejchar P, Potocký M, Sekereš J, Žárský V, Kulich I. *Arabidopsis* trichome contains two plasma membrane domains with different lipid compositions which attract distinct EXO70 subunits. Int J Mol Sci. 2019:**20**(15):3803. https://doi.org/10.3390/ijms20153803

Kulich I, Cole R, Drdová E, Cvrcková F, Soukup A, Fowler J, Žárský V. Arabidopsis exocyst subunits SEC8 and EXO70A1 and exocyst interactor ROH1 are involved in the localized deposition of seed coat pectin. New Phytol. 2010:**188**(2):615–625. https://doi.org/10.1111/j.1469-8137.2010.03372.x

Kulich I, Vojtíková Z, Glanc M, Ortmannová J, Rasmann S, Žárský V. Cell wall maturation of Arabidopsis trichomes is dependent on exocyst subunit EXO70H4 and involves callose deposition. Plant Physiol. 2015:**168**(1):120–131. https://doi.org/10.1104/pp.15.00112

Kulich I, Vojtíková Z, Sabol P, Ortmannová J, Neděla V, Tihlaříková E, Žárský V. Exocyst subunit EXO70H4 has a specific role in callose synthase secretion and silica accumulation. Plant Physiol. 2018:**176**(3):2040–2051. https://doi.org/10.1104/pp.17.01693

Kusch S, Panstruga R. *mlo*-based resistance: an apparently universal "weapon" to defeat powdery mildew disease. Mol Plant Microbe Interact. 2017:**30**(3):179–189. https://doi.org/10.1094/MPMI-12-16-0255-CR

Kusch S, Pesch L, Panstruga R. Comprehensive phylogenetic analysis sheds light on the diversity and origin of the MLO family of integral membrane proteins. Genome Biol Evol. 2016:**8**(3):878–895. https://doi.org/10.1093/gbe/evw036

Kwon C, Neu C, Pajonk S, Yun HS, Lipka U, Humphry M, Bau S, Straus M, Kwaaitaal M, Rampelt H, et al. Co-option of a default secretory pathway for plant immune responses. Nature. 2008a:**451**(7180):835–840. https://doi.org/10.1038/nature06545

Kwon C, Panstruga R, Schulze-Lefert P. Les liaisons dangereuses: immunological synapse formation in animals and plants. Trends Immunol. 2008b:**29**(4):159–166. https://doi.org/10.1016/j.it.2008.01.004

Lalonde S, Ehrhardt DW, Loqué D, Chen J, Rhee SY, Frommer WB. Molecular and cellular approaches for the detection of protein–protein interactions: latest techniques and current limitations. Plant J. 2008:**53**(4):610–635. https://doi.org/10.1111/j.1365-313X.2007.03332.x

Larson ER, Ortmannová J, Donald NA, Alvim J, Blatt MR, Žárský V. Synergy among exocyst and SNARE interactions identifies a functional hierarchy in secretion during vegetative growth. Plant Cell. 2020:**32**(9):2951–2963. https://doi.org/10.1105/tpc.20.00280

Lê S, Josse J, Husson F. FactoMineR: an R package for multivariate analysis. J Stat Soft. 2008:**25**(1):1–18. https://doi.org/10.18637/jss.v025.i01

Lei Y, Lu L, Liu H-Y, Li S, Xing F, Chen L-L. CRISPR-P: a web tool for synthetic single-guide RNA design of CRISPR-system in plants. Mol Plant. 2014:**7**(9):1494–1496. https://doi.org/10.1093/mp/ssu044

Mann HB, Whitney DR. On a test of whether one of two random variables is stochastically larger than the other. Ann Math Statist. 1947:**18**(1):50–60. https://doi.org/10.1214/aoms/1177730491

Marks MD, Wenger JP, Gilding E, Jilk R, Dixon RA. Transcriptome analysis of *Arabidopsis* wild-type and *gl3-sst sim* trichomes identifies four additional genes required for trichome development. Mol Plant. 2009:**2**(4):803–822. https://doi.org/10.1093/mp/ssp037

Martin KJ, McGhee EJ, Schwarz JP, Drysdale M, Brachmann SM, Stucke V, Sansom OJ, Anderson KI. Accepting from the best donor; analysis of long-lifetime donor fluorescent protein pairings to optimise dynamic FLIM-based FRET experiments. PLoS One. 2018:**13**(1):e0183585. https://doi.org/10.1371/journal.pone.0183585

Meng J-G, Liang L, Jia P-F, Wang Y-C, Li H-J, Yang W-C. Integration of ovular signals and exocytosis of a Ca^{2+} channel by MLOs in pollen tube guidance. Nat Plants. 2020:**6**(2):143–153. https://doi.org/10.1038/s41477-020-0599-1

Meyer D, Pajonk S, Micali C, O'Connell R, Schulze-Lefert P. Extracellular transport and integration of plant secretory proteins into pathogen-induced cell wall compartments. Plant J. 2009:**57**(6):986–999. https://doi.org/10.1111/j.1365-313X.2008.03743.x

Michalopoulou VA, Mermigka G, Kotsaridis K, Mentzelopoulou A, Celie PHN, Moschou PN, Jones JDG, Sarris PF. The host exocyst complex is targeted by a conserved bacterial type-III effector that promotes virulence. Plant Cell. 2022:**34**(9):3400–3424. https://doi.org/10.1093/plcell/koac162

Nishimura MT, Stein M, Hou BH, Vogel JP, Edwards H, Somerville SC. Loss of a callose synthase results in salicylic acid-dependent disease resistance. Science. 2003:**301**(5635):969–972. https://doi.org/10.1126/science.1086716

Ortmannová J, Sekereš J, Kulich I, Šantrůček J, Dobrev P, Žárský V, Pečenková T. Arabidopsis EXO70B2 exocyst subunit contributes to papillae and encasement formation in antifungal defence. J Exp Bot. 2022:**73**(3):742–755. https://doi.org/10.1093/jxb/erab457

Pang ZP, Südhof TC. Cell biology of Ca^{2+}-triggered exocytosis. Curr Opin Cell Biol. 2010:**22**(4):496–505. https://doi.org/10.1016/j.ceb.2010.05.001

Pearson K. X. On the criterion that a given system of deviations from the probable in the case of a correlated system of variables is such that it can be reasonably supposed to have arisen from random sampling. Lond Edinb Dubl Phil Mag J Sci. 1900:**50**(302):157–175. https://doi.org/10.1080/14786440009463897

Pečenková T, Hala M, Kulich I, Kocourkova D, Drdova E, Fendrych M, Toupalova H, Žárský V. The role for the exocyst complex subunits Exo70B2 and Exo70H1 in the plant–pathogen interaction. J Exp Bot. 2011:**62**(6):2107–2116. https://doi.org/10.1093/jxb/erq402

Pečenková T, Markovic V, Sabol P, Kulich I, Žárský V. Exocyst and autophagy-related membrane trafficking in plants. J Exp Bot. 2017:**69**(1):47–57. https://doi.org/10.1093/jxb/erx363

Piffanelli P, Zhou F, Casais C, Orme J, Jarosch B, Schaffrath U, Collins NC, Panstruga R, Schulze-Lefert P. The barley MLO modulator of defense and cell death is responsive to biotic and abiotic stress stimuli. Plant Physiol. 2002:**129**(3):1076–1085. https://doi.org/10.1104/pp.010954

Pradhan Mitra P, Loqué D. Histochemical staining of *Arabidopsis thaliana* secondary cell wall elements. J Vis Exp. 2014:(87):51381. https://doi.org/10.3791/51381

Ricachenevsky FK, Punshon T, Salt DE, Fett JP, Guerinot ML. *Arabidopsis thaliana* zinc accumulation in leaf trichomes is correlated with zinc concentration in leaves. Sci Rep. 2021:**11**(1):5278. https://doi.org/10.1038/s41598-021-84508-y

Rossi G, Lepore D, Kenner L, Czuchra AB, Plooster M, Frost A, Munson M, Brennwald P. Exocyst structural changes associated with activation of tethering downstream of Rho/Cdc42 GTPases. J Cell Biol. 2020:**219**(2):e201904161. https://doi.org/10.1083/jcb.201904161

Schindelin J, Arganda-Carreras I, Frise E, Kaynig V, Longair M, Pietzsch T, Preibisch S, Rueden C, Saalfeld S, Schmid B, et al. Fiji: an open-source platform for biological-image analysis. Nat Methods. 2012:**9**(7):676–682. https://doi.org/10.1038/nmeth.2019

Schmelzer E. Cell polarization, a crucial process in fungal defence. Trends Plant Sci. 2002:**7**(9):411–415. https://doi.org/10.1016/S1360-1385(02)02307-5

Sekereš J, Pejchar P, Šantrůček J, Vukašinović N, Žárský V, Potocký M. Analysis of exocyst subunit EXO70 family reveals distinct membrane polar domains in tobacco pollen tubes. Plant Physiol. 2017:**173**(3):1659–1675. https://doi.org/10.1104/pp.16.01709

Seregin IV, Ivanov VB. Histochemical investigation of cadmium and lead distribution in plants. Russ J Plant Physiol. 1997:**44**(6):791–796.

Shapiro SS, Wilk MB. An analysis of variance test for normality (complete samples). Biometrika. 1965:**52**(3–4):591–611. https://doi.org/10.1093/biomet/52.3-4.591

Stegmann M, Anderson RG, Westphal L, Rosahl S, McDowell JM, Trujillo M. The exocyst subunit *Exo70B1* is involved in the immune response of *Arabidopsis thaliana* to different pathogens and cell death. Plant Signal Behav. 2013:**8**(12):e27421. https://doi.org/10.4161/psb.27421

Stein M, Dittgen J, Sanchez-Rodriguez C, Hou BH, Molina A, Schulze-Lefert P, Lipka V, Somerville S. *Arabidopsis* PEN3/PDR8, an ATP binding cassette transporter, contributes to nonhost resistance to inappropriate pathogens that enter by direct penetration. Plant Cell. 2006:**18**(3):731–746. https://doi.org/10.1105/tpc.105.038372

Student. The probable error of a mean. Biometrika. 1908:**6**(1):1–25. https://doi.org/10.2307/2331554

Synek L, Pleskot R, Sekereš J, Serrano N, Vukašinović N, Ortmannová J, Klejchová M, Pejchar P, Batystová K, Gutkowska M, et al. Plasma membrane phospholipid signature recruits the plant exocyst complex via the EXO70A1 subunit. Proc Natl Acad Sci U S A. 2021:**118**(36):e2105287118. https://doi.org/10.1073/pnas.2105287118

Synek L, Schlager N, Eliás M, Quentin M, Hauser M-T, Žárský V. AtEXO70A1, a member of a family of putative exocyst subunits specifically expanded in land plants, is important for polar growth and plant development. Plant J. 2006:**48**(1):54–72. https://doi.org/10.1111/j.1365-313X.2006.02854.x

Szymanski DB, Jilk RA, Pollock SM, Marks MD. Control of *GL2* expression in *Arabidopsis* leaves and trichomes. Development. 1998:**125**(7):1161–1171. https://doi.org/10.1242/dev.125.7.1161

TerBush DR, Maurice T, Roth D, Novick P. The exocyst is a multiprotein complex required for exocytosis in *Saccharomyces cerevisiae*. EMBO J. 1996:**15**(23):6483–6494. https://doi.org/10.1002/j.1460-2075.1996.tb01039.x

Thomas M, Huck N, Hoehenwarter W, Conrath U, Beckers GJM. Combining metabolic ^{15}N labeling with improved tandem MOAC for enhanced probing of the phosphoproteome. In: **Schulze WX**, editors. Plant phosphoproteomics. New York (NY): Springer New York; 2015. p. 81–96.

van Leeuwen W, Vermeer JEM, Gadella TW Jr, Munnik T. Visualization of phosphatidylinositol 4,5-bisphosphate in the plasma membrane of suspension-cultured tobacco BY-2 cells and whole Arabidopsis seedlings. Plant J. 2007:**52**(6):1014–1026. https://doi.org/10.1111/j.1365-313X.2007.03292.x

Vogel JP, Raab TK, Schiff C, Somerville SC. PMR6, a pectate lyase-like gene required for powdery mildew susceptibility in Arabidopsis. Plant Cell. 2002:**14**(9):2095–2106. https://doi.org/10.1105/tpc.003509

Vogel JP, Raab TK, Somerville CR, Somerville SC. Mutations in PMR5 result in powdery mildew resistance and altered cell wall composition. Plant J. 2004:**40**(6):968–978. https://doi.org/10.1111/j.1365-313X.2004.02264.x

Vogel J, Somerville S. Isolation and characterization of powdery mildew-resistant Arabidopsis mutants. Proc Natl Acad Sci U S A. 2000:**97**(4):1897–1902. https://doi.org/10.1073/pnas.030531997

Wang W, Liu N, Gao C, Cai H, Romeis T, Tang D. The Arabidopsis exocyst subunits EXO70B1 and EXO70B2 regulate FLS2 homeostasis at the plasma membrane. New Phytol. 2020:**227**(2):529–544. https://doi.org/10.1111/nph.16515

Wang W, Liu N, Gao C, Rui L, Tang D. The *Pseudomonas syringae* effector AvrPtoB associates with and ubiquitinates *Arabidopsis* exocyst subunit EXO70B1. Front Plant Sci. 2019:**10**:1027. https://doi.org/10.3389/fpls.2019.01027

Wei T, Simko V. R package 'corrplot': Visualization of a correlation matrix (version 0.92). 2021. https://github.com/taiyun/corrplot

Wickham H, Averick M, Bryan J, Chang W, McGowan L, François R, Grolemund G, Hayes A, Henry L, Hester J, et al. Welcome to the Tidyverse. J Open Source Softw. 2019:**4**(43):1686. https://doi.org/10.21105/joss.01686

Winter D, Vinegar B, Nahal H, Ammar R, Wilson GV, Provart NJ, Baxter I. An "Electronic Fluorescent Pictograph" browser for exploring and analyzing large-scale biological data sets. PLoS ONE. 2007:**2**(8):e718. https://doi.org/10.1371/journal.pone.0000718

Wolter M, Hollricher K, Salamini F, Schulze-Lefert P. The *mlo* resistance alleles to powdery mildew infection in barley trigger a developmentally controlled defence mimic phenotype. Mol Gen Genet. 1993:**239**(1–2):122–128. https://doi.org/10.1007/BF00281610

Wood PJ. Specificity in the interaction of direct dyes with polysaccharides. Carbohydr Res. 1980:**85**(2):271–287. https://doi.org/10.1016/S0008-6215(00)84676-5

Xing H-L, Dong L, Wang Z-P, Zhang H-Y, Han C-Y, Liu B, Wang X-C, Chen Q-J. A CRISPR/Cas9 toolkit for multiplex genome editing in plants. BMC Plant Biol. 2014:**14**(1):327. https://doi.org/10.1186/s12870-014-0327-y

Yeats T, Vellosillo T, Sorek N, Ibáñez A, Bauer S. Rapid determination of cellulose, neutral sugars, and uronic acids from plant cell walls by one-step two-step hydrolysis and HPAEC-PAD. Bio Protoc. 2016:**6**(20):e1978. https://doi.org/10.21769/BioProtoc.1978

Yun HS, Panstruga R, Schulze-Lefert P, Kwon C. Ready to fire: secretion in plant immunity. Plant Signal Behav. 2008:**3**(7):505–508. https://doi.org/10.4161/psb.3.7.6098

Žárský V, Sekereš J, Kubátová Z, Pečenková T, Cvrčková F. Three subfamilies of exocyst EXO70 family subunits in land plants: early divergence and ongoing functional specialization. J Exp Bot. 2020:**71**(1):49–62. https://doi.org/10.1093/jxb/erz423

Zhao T, Rui L, Li J, Nishimura MT, Vogel JP, Liu N, Liu S, Zhao Y, Dangl JL, Tang D. A truncated NLR protein, TIR-NBS2, is required for activated defense responses in the *exo70B1* mutant. PLoS Genet. 2015:**11**(1):e1004945. https://doi.org/10.1371/journal.pgen.1004945